1
2

AIM2 inflammasome activation in astrocytes occurs during the late phase

of EAE

5
6

7 William E. Barclay[a], M. Elizabeth Deerhake[a], Makoto Inoue[a,b], Toshiaki Nonaka[a], Kengo Nozaki[a], Nathan
8 A. Luzum[a], Nupur Aggarwal[a], Edward A. Miao [a,c], Mari L. Shinohara[a,c,*]
9
10 [a]Department of Immunology, Duke University Medical School. Durham, NC 27710.
11 [b]Department of Comparative Biosciences, University of Illinois at Urbana-Champaign, Urbana, IL 61802.
12 [c]Department of Molecular Genetics and Microbiology, Duke University Medical School. Durham, NC
13 27710.
14
15
16
17
18 **Corresponding Author:** Mari L. Shinohara
19 mari.shinohara@duke.edu
20
21 **Keywords:** Experimental autoimmune encephalomyelitis (EAE); AIM2 inflammasome; astrocytes; ASC
22 specks
23
24
25

ABSTRACT

Inflammasomes are a class of innate immune signaling platforms that activate in response to an array of cellular damage and pathogens. Inflammasomes promote inflammation under many circumstances to enhance immunity against pathogens and inflammatory responses through their effector cytokines, IL-1β and IL-18. Multiple sclerosis and its animal model, experimental autoimmune encephalomyelitis (EAE), are such autoimmune conditions influenced by inflammasomes. Despite work investigating inflammasomes during EAE, little remains known concerning the role of inflammasomes in the central nervous system (CNS) during the disease. Here we use multiple genetically modified mouse models to monitor activated inflammasomes *in situ* based on ASC oligomerization in the spinal cord. Using inflammasome reporter mice, we found heightened inflammasome activation in astrocytes after the disease peak. In contrast, microglia and CNS-infiltrated myeloid cells had few activated inflammasomes in the CNS during EAE. Astrocyte inflammasome activation was dependent on AIM2, but low IL-1β expression and no significant signs of cell death were found in astrocytes during EAE. Thus, the AIM2 inflammasome activation in astrocytes may have a distinct role from traditional inflammasome-mediated inflammation.

SIGNIFICANCE STATEMENT

Inflammasome activation in the peripheral immune system is pathogenic in multiple sclerosis (MS) and its animal model, experimental autoimmune encephalomyelitis (EAE). However, inflammasome activity in the central nervous system (CNS) is largely unexplored. Here, we used genetically modified mice to determine inflammasome activation in the CNS during EAE. Our data indicated heightened AIM2 inflammasome activation in astrocytes after the disease peak. Unexpectedly, neither CNS-infiltrated myeloid cells nor microglia were the primary cells with activated inflammasomes in SC during EAE. Despite AIM2 inflammasome activation, astrocytes did not undergo apparent cell death and produced little of the proinflammatory cytokine, IL-1β, during EAE. This study showed that CNS inflammasome activation occurs during EAE without associating with IL-1β-mediated inflammation.

INTRODUCTION

Multiple sclerosis (MS) and its mouse model, experimental autoimmune encephalomyelitis (EAE), are demyelinating neurodegenerative diseases punctuated by inflammatory immune reactions in the central nervous system (CNS). Inflammasomes are sensors of a wide range of microbe-associated molecular patterns (MAMPs) and damage-associated molecular patterns (DAMPs) and induce inflammation (1). In EAE, the NLRP3 inflammasome has a particularly well-documented role in the peripheral immune system in promoting immune cell recruitment to the CNS through the generation of the inflammatory cytokines IL-1β and IL-18 by peripheral myeloid cells (2-5). However, despite much work centered on inflammasomes in the peripheral immune response, the role of inflammasomes in the CNS is significantly less understood.

Inflammasomes are distinct from other PRRs in mode of signaling and downstream effector function. First, a sensor (*e.g.,* NLRP3, AIM2) forms a scaffold, to which the inflammasome adaptor ASC binds and polymerizes (called the "ASC speck"). Pro-caspase-1 associates with the polymer, then self-cleaves to become proteolytically active caspase-1, which further activates downstream substrates, including pro-IL-1β, pro-IL-18, and the pore-forming protein, gasdermin-D (GSDMD). Cleaved GSDMD forms a pore in cellular membranes and induces pyroptosis, resulting in a release of mature IL-1β and IL-18 to the extracellular space. In MS, genetic variation in inflammasome signaling pathways was reported (6, 7). Particularly, the NLRP3 inflammasome was demonstrated to be a prognostic factor and a therapeutic target in primary progressive MS (8). In EAE, NLRP3 and ASC are necessary for passive and standard ("Type-A") active EAE (2-

75   4). NLRP3 inflammasome activation in macrophages and dendritic cells in secondary lymphoid
76   organs results in IL-1β and IL-18 release, which induces expression of chemokines and their
77   receptors required for leukocyte CNS entry (2). We have also demonstrated that the NLRP3
78   inflammasome can be dispensable for EAE induction if the innate immune system is strongly
79   activated with aggressive immunization schemes ("Type-B EAE")(9).
80   As inflammasome activation is a post-translational process, the expression of
81   inflammasome components does not necessarily indicate their activation. Thus, separately
82   assessing both expression and activation of inflammasomes is critical. Recent studies indicated
83   that microglia, astrocytes, and neurons can activate inflammasomes; and most identification was
84   performed *ex vivo* (8, 10-17). However, defining inflammasome activation *in situ* is critical
85   because CNS-resident cells significantly alter their behavior once isolated from tissues. So far,
86   only a limited number of studies has demonstrated unequivocal activation of inflammasomes *in
87   situ* in the CNS (10-12).
88   In this report, we identified activated inflammasomes in the CNS during EAE using the
89   ASC-Citrine mouse line, which allows *in situ* detection of activated inflammasomes (18). Our study
90   identified maximal inflammasome activation in the spinal cord (SC) after the EAE peak, which
91   contrasts with the inguinal lymph nodes (iLNs), in which inflammasome activation was present at
92   pre-symptomatic disease. Unexpectedly, neither microglia nor CNS-infiltrated myeloid cells were
93   the primary cells with activated inflammasomes in SC during EAE. Instead, we detected
94   inflammasome activation mainly in astrocytes and limited inflammasome activation in motor
95   neurons. Furthermore, we found that the AIM2 inflammasome is activated in astrocytes during
96   EAE. However, even with AIM2 inflammasome activation, astrocytes did not clearly undergo cell
97   death and have poor *Il1b* gene expression, suggesting the possibility that AIM2 inflammasome
98   activation in astrocytes serves a different purpose than traditional inflammasome-mediated
99   inflammation.
100

101   **RESULTS**
102

103   **Inflammasome activation in the spinal cord at a late stage of EAE**
104   Inflammasome signaling is critical to EAE development in the peripheral lymphoid organs
105   (2-5, 9). Yet, the extent and spatiotemporal distribution of inflammasome activation in the CNS
106   during EAE is largely unknown. Classically, detection of inflammasome activation is performed
107   by identifying cleaved caspase-1 by Western blotting (WB), which cannot be applied *in situ*.
108   Therefore, we used a different molecular signature of inflammasome activation – the
109   oligomerization of ASC, microscopically observed as the "ASC speck." In this study, we used
110   inflammasome activation reporter mice, which express ASC fused to a fluorescent Citrine protein
111   (ASC-Citrine)(18). The ASC-Citrine reporter allows *in situ* detection of active inflammasomes by
112   visualization of ASC specks (12, 18) (**Fig. S1*A***), and the presence of the reporter did not alter
113   disease course of EAE (**Fig. 1*A***). The ASC-Citrine reporter was validated for use in tissue by
114   immunostaining against ASC in live spleen slice cultures following NLRP3 inflammasome
115   activation (**Fig. S1*A***).
116   Before evaluating inflammasome activation in the CNS, we first visualized and quantified
117   ASC specks in the iLNs as the primary site of immune reaction to EAE induction. ASC specks
118   were detected at 3 days post induction (dpi) of EAE (**Fig. 1*B, C***), which is well before the disease
119   onset, and continually detected until 9-dpi (**Fig. 1*C***). However, ASC specks were almost
120   undetectable by the point of disease peak (16-dpi) and after (**Fig. 1*C***). The cervical lymph nodes
121   (cLN) have also been noted as a site of primary immune reaction in some models of EAE (19,
122   20), but few ASC specks were detected there throughout disease (**Fig, S1B**). The spinal cord
123   (SC) of ASC-Citrine mice exhibited a much higher number of ASC specks than the iLNs (**Fig. 1*D-***

124 *F*) with a significant increase in the number of ASC specks in the later phase of EAE at 30-dpi
125 (**Fig. 1*D, F***). Further, in addition to ASC specks, we also observed atypical fiber-like ASC-Citrine
126 signals, which we termed "ASC strings," unique to the CNS (**Fig. 1*G***). While different in
127 magnitude, both ASC specks and ASC strings appeared with the largest increases at the later
128 phase of disease, around 30-dpi (**Fig. 1*F, H***). Due to the abundance of ASC specks and strings
129 at 30-dpi, all subsequent analyses in SC were at 30-dpi, unless otherwise stated. This
130 quantification was also performed manually, and all subsequent ASC speck and string
131 quantification was performed using the Imaris software.
132 We have previously shown a sub-type of EAE (Type-B EAE) which does not require the
133 NLRP3 inflammasome in the peripheral lymphoid organs to develop EAE (9). In the CNS, Type-
134 A and Type-B EAE had comparable numbers of ASC specks (**Fig. S1*C, D***), suggesting the more
135 consistent connection of EAE severity and active inflammasome in the CNS than in the periphery.
136 In sum, these results suggest that inflammasomes are activated in the SC during both Type-A
137 and Type-B EAE and that their activation is heightened after peak disease.
138
Inflammasome activation in non-BM-derived cells in the spinal cord
140 Because we identified inflammasome activation in the CNS during EAE, the role of ASC
141 in non-hematopoietic cells was investigated with a bone marrow (BM) chimera approach using
142 CD45.1 congenic donor mice. We compared two groups of BM chimeras, generated by adoptively
143 transferring WT BM cells to either WT or *Pycard*^{-/-} (ASC knockout) recipients (the extent of
144 reconstitution is shown in **Fig. S2*A***). Compared to WT recipients, *Pycard*^{-/-} recipients
145 demonstrated milder EAE after the disease peak (**Fig. 2*A-C***), suggesting that ASC in non-
146 hematopoietic cells impacted EAE severity after the disease peak. Next, we sought to determine
147 if CNS-infiltrated cells possess activated inflammasomes in the SC during EAE. Two groups of
148 BM chimeras were compared; one group with ASC-Citrine BM donor cells to wild-type (WT)
149 recipients and the other with WT BM cells to ASC-Citrine recipients. Reconstitution of
150 approximately 90% of BM cells were confirmed (**Fig. S2*B***) and no impact of ASC-Citrine
151 expression on EAE development was confirmed (**Fig. S2*C***). ASC specks were identified in the
152 iLNs of WT recipients reconstituted with ASC-Citrine BM (**Fig. 2*D, E***). However, unexpectedly,
153 the mice showed no ASC specks and strings in the SC (**Fig. 2*F-H***; **S2*D***). In contrast, ASC specks
154 and strings were identified in the SC of ASC-Citrine recipients transferred with WT BM cells (**Fig.
155 2*F-H***). This suggests that the source of inflammasome activation is CNS-resident cells in the SC.
156
Inflammasome activation in CNS during EAE in astrocytes
158 We next sought to identify CNS-resident cells with activated inflammasomes during EAE.
159 ASC specks and strings were identified, and then cell types were assigned by counterstaining to
160 identify microglia (TMEM119), astrocytes (GFAP or ALDH1L1), neurons (NeuN), oligodendrocyte
161 precursor cells (NG2), or mature oligodendrocytes (MBP) (**Fig. 3*A-C*; S2*E, F***). The majority of
162 ASC specks and strings were found in astrocytes, while a small number were classified as
163 microglial and neuronal (**Fig. 3*D-F***). Few ASC specks or strings were detected in oligodendrocyte
164 precursor cells (OPCs) or mature oligodendrocytes (**Fig. S2*G, H***). In neurons, all ASC specks
165 were found in cell bodies of ChAT[+] alpha motor neurons (ChAT[+]NeuN[+]) in the ventral horn (VH),
166 but these neuronal ASC specks did not increase during EAE (**Fig. S2*I***).
167 We further validated these findings with a cell type-specific ASC-Citrine reporter approach
168 by using *Asc-Citrine*[LSL] mice, which retain an LSL cassette upstream of the ASC-Citrine construct.
169 To express ASC-Citrine in astrocytes and neurons in a cell type-specific manner, we used
170 *Gfap*[Cre]*;Asc-Citrine*[LSL] and *Syn1*[Cre]*;Asc-Citrine*[LSL] mice, respectively. For microglia-specific ASC-
171 Citrine expression, we used *Cx3cr1*[CreERT2]*;Asc-Citrine*[LSL] mice treated with tamoxifen (TAM) with
172 a six-week "wash out" period to exclude ASC-citrine expression in myeloid cells other than
173 microglia (**Fig. S3*A***) by taking an advantage of the long half-life of microglia (gating strategy to

174   evaluate microglia is shown in **Fig. S3B**). We considered that using the microglia-specific ASC-
175   Citrine reporter mice was critical because the expression level of Tmem119, used in **Fig. 3A-F**,
176   decreases as EAE progresses (21) and may confound some image analysis. No alteration in EAE
177   severity was confirmed in the group of mutant mice expressing Cre in targeted cell types (**Fig.
178   S3C-E**). The SC of these mutant mice was analyzed during EAE by confocal microscopy (**Fig.
179   4A-C**). Again, a high number of ASC specks and strings were confirmed in astrocytes by using
180   the *Gfap^{Cre};Asc-Citrine^{LSL}* mice, while few ASC specks or strings were identified in microglia (**Fig.
181   4D, E**). Neurons also showed a consistent but small number of ASC specks (**Fig. 4D, E**).
182   Nonetheless, these data mirrored the results by antibody counterstaining in **Fig. 3A-G**, strongly
183   indicating that inflammasome activation is predominantly in astrocytes during EAE.
184
185   **Limited induction of IL-1β-mediated inflammation by astrocytes during EAE**
186   In EAE, astrocytes become activated in a process called astrogliosis; these activated cells
187   gain a pro-inflammatory phenotype and are termed "reactive astrocytes" (22, 23). Here we
188   investigated whether astrogliosis correlates with inflammasome activation. Astrogliosis was
189   detected as increased GFAP intensity at 30-dpi (**Fig. 5A, B**), but GFAP intensity did not correlate
190   on a per cell basis with the presence of ASC specks (**Fig. 5C, D**). We similarly found no correlation
191   between inflammasome activation and individual acquisition of the neurotoxic "A1" reactive
192   astrocyte phenotype (24, 25), based on the A1-astrocyte marker C3d (26), although C3d
193   expression was enhanced in astrocytes in aggregate during EAE (**Fig. 5C, E**).
194   To evaluate astrocyte gene expression during EAE, we first re-analyzed publicly available
195   data obtained with a *Gfap^{Cre}*-driven RiboTag mouse system, which allows purification of astrocyte-
196   specific RNA (GSE100329)(27). Gene expression in total SC and SC astrocytes were compared
197   between naïve and 30-dpi EAE mice. We found low expression of *Il1b* and genes encoding
198   inflammasome sensor proteins (**Fig. S4A**). Expression levels of *Il18* and *Casp1* were enriched in
199   astrocytes independent of EAE (**Fig. S4A**). To validate this data, we evaluated gene expression
200   by RT-qPCR in total SC cells and astrocytes enriched by bead selection from naïve and 30-dpi
201   EAE mice. Astrocyte-enriched cells showed generally low expression of genes encoding proteins
202   related to inflammasomes even during EAE. Notably, the expression of *Il1b, Casp-1*, and *Gsdmd*
203   was significantly lower in astrocyte-enriched cells than total SC cells (normalized to *Il1b* and
204   *Casp1* expression in naïve total SC cells for **Fig. 6A** and **B**, respectively). In the qPCR analyses,
205   a majority of genes shown in **Fig. S4A** had mRNA levels that were close to the detection limit,
206   despite reasonably high total RNA amounts, suggesting the general low expression of
207   inflammasome-related genes in astrocytes. Under the low gene expression, we did not observe
208   astrocyte enrichment of *Il18* and *Casp1* expression, as suggested in the RiboTag data (**Fig. S4A**).
209   This was consistent with the limited detection of the inflammasome-related proteins caspase-1,
210   IL-1β, and GSDMD in SC astrocytes of either naïve mice or mice with EAE 30 dpi by
211   immunostaining, despite robust detection in the spleen (**Fig. S4B-G**). However, mild expression
212   of GSDMD was detected in SC astrocytes following EAE induction (**Fig. S4D, G**). Next, we
213   performed Western blotting (WB) to evaluate protein levels and inflammasome activation *in vitro*.
214   Here, we used the C8-S astrocyte cell line due to the difficulty of culturing primary astrocytes,
215   especially without altering their character in tissue culture settings. We compared C8-S to bone
216   marrow-derived macrophages (BMDMs) as a positive control. We stimulated the NLRP3 or AIM2
217   inflammasome with nigericin or poly(dA:dT)-liposomes, respectively, after ultrapure LPS pre-
218   treatment. Culture supernatants of C8-S showed a scarcity of cleaved caspase-1, IL-1β and IL-
219   18 (**Fig. 6C; S5A-C**). Notably, C8-S cell lysates also showed greatly reduced pro-caspase-1, pro-
220   IL-1β, GSDMD-FL, and GSDMD-NT, compared to BMDMs (**Fig. 6C; S5D-H**). These results
221   suggest that astrocytes do not induce inflammation, mediated particularly by IL-1β as
222   macrophages do.

223   Next, we investigated whether astrocytes with ASC specks or strings undergo cell death
224   during EAE. We attempted to assess general cell death by TUNEL staining. TUNEL$^+$ cells were
225   present in the periphery of the SC at 30-dpi EAE, though no TUNEL$^+$ astrocytes were detected
226   (**Fig. 6D, E**), consistent with previous data demonstrating that astrocytes do not undergo
227   significant cell death during EAE (28). Although normally not associated with canonical
228   inflammasomes, we found enriched active caspase-3 (CC3) in astrocytes with active
229   inflammasomes in both ASC-Citrine (**Fig. 6F, G**) and *Gfap^{Cre};Asc-Citrine^{LSL}* (**Fig. S5I**) mice,
230   suggesting a possible connection between inflammasomes and caspase-3 activation in
231   astrocytes. In summary, inflammasomes activation in astrocytes does not appear to lead to typical
232   outcomes of inflammasome activation as seen in myeloid cells.
233
234   **AIM2 facilitates inflammasome activation in the CNS during EAE**
235   To further assess which inflammasome is activated in astrocytes during EAE, we selected
236   NLRP3 and AIM2 among the inflammasome sensors based on their expression by astrocytes
237   during EAE by the Ribotag raw transcript data (**Fig. S4A**). As *Nlrp3$^{-/-}$* mice are resistant to
238   standard EAE, we used the Type-B EAE model to induce EAE in the *Nlrp3$^{-/-}$* background (3, 9)
239   and confirmed that ASC-Citrine mice and *Nlrp3$^{-/-}$;*ASC-Citrine developed similar disease course
240   and severity, as expected (**Fig. S6A**). Here, *Nlrp3$^{-/-}$*; ASC-Citrine mice still showed comparable
241   numbers of ASC specks with ASC-Citrine mice (**Fig. 7A**, **B**), suggesting that NLRP3 is
242   dispensable in CNS inflammasome activation during EAE. Next, we tested the AIM2
243   inflammasome. Congruent with recent reports (13, 29), we found AIM2 to be protective in EAE,
244   as demonstrated by more severe disease in *Aim2$^{-/-}$* mice predominantly after disease peak, when
245   induced with a low dose adjuvant (50 μg *Mtb*/mouse) (**Fig. 7C, D**). The immune phenotype of
246   *Aim2$^{-/-}$* mice in SC, iLN, and spleen at 16-dpi did not show statistically significant changes
247   compared to WT mice, although a trend of increased T cells, microglia, and macrophages were
248   observed, possibly reflecting the disease severity of *Aim2$^{-/-}$* mice (**Fig. S6B-D**), together with
249   enhanced astrogliosis (**Fig. S6E, 7E**).
250   Next, we investigated the role of the AIM2 in astrocyte inflammasome activation during
251   EAE. To do so, we sought an EAE condition for *Aim2$^{-/-}$* mice to develop comparable EAE severity.
252   Despite increased EAE severity in *Aim2$^{-/-}$* mice, an increased adjuvant dose (200 μg *Mtb*/mouse)
253   elicited comparable EAE scores between WT and *Aim2$^{-/-}$* mice (**Fig. 7F**). Here, a strong gene
254   dosage effect of AIM2 on ASC speck formation was observed (**Fig. 7G, H**), strongly suggesting
255   that inflammasome activation in astrocytes *in vivo* indeed requires AIM2.
256
257
258   **DISCUSSION**
259   Many studies show gene and protein expression of inflammasome components in the
260   CNS *in vivo*, but a few have evaluated *bona fide* inflammasome activation. This study used
261   reporter mice to detect activated inflammasomes *in situ* in a cell-type-specific manner in the CNS
262   during EAE. Using the ASC-Citrine mice, we identified AIM2 inflammasome activation after
263   disease peak mainly in astrocytes in the SC of EAE mice. Unexpectedly, we detected limited or
264   no inflammasome activation in CNS-infiltrated myeloid cells or microglia.
265   Previous studies suggested inflammasome activation in CNS-resident cells during EAE
266   and MS, but these studies evaluated inflammasome activation of microglia or astrocytes in tissue
267   culture (8, 13-17). A few studies demonstrated inflammasome activation in the CNS during EAE
268   *in situ*. One such study showed ASC specks in Iba-1$^+$ cells, suggested to be microglia, in the
269   hippocampus of EAE mice, but the investigation was not extended to astrocytes (11). Another
270   study suggested caspase-8-mediated noncanonical NLRP3 inflammasome activation in microglia
271   in the SC of EAE mice based on caspase-8-FLICA staining of tissue sections (30). It is possible

272 that a small number of microglia may activate inflammasomes, although our data showed that
273 significantly more inflammasome activation occurs at 30-dpi in astrocytes.
274   We and other groups have shown that the NLRP3 inflammasome is detrimental in EAE.
275 However, recent studies (13, 29) and our results demonstrate that AIM2 can play a protective
276 role. Chou et al. demonstrated that AIM2 suppresses EAE by promoting T_{reg} stability in an
277 inflammasome-independent fashion (29). Similarly, the study by Ma et al. demonstrated a
278 protective role of AIM2 through another inflammasome-independent mechanism targeting the
279 DNA-PK-AKT3 pathway (13). Using $Aim2^{fl/fl};Gfap^{Cre}$ mice, Ma et al. evaluated the disease severity
280 in Type-B EAE and found that astrocyte-specific *Aim2* depletion did not change the disease
281 severity (13). Of note, the study did not evaluate the disease score beyond 18 dpi (around disease
282 peak) (13). However, our data indicated numbers of ASC specks both in naïve and 16-dpi EAE
283 mice (around disease peak) are basal, while the most significant increase was observed on 30-
284 dpi. Additionally, Ma et al. induced Type-B EAE in $Aim2^{fl/fl};Gfap^{Cre}$ mice (13) but we did not. Thus,
285 intensity of EAE induction possibly affects the involvement of AIM2 in EAE too, as we
286 demonstrated that increased adjuvant upon induction of EAE blunts the impact of AIM2 on
287 disease (**Fig. 7F**). A long-term evaluation of astrocyte-specific AIM2 knockout mice and
288 elucidating an impact of EAE induction methods will merit further understanding the protective
289 role of the AIM2 inflammasomes in astrocytes.
290   Using the ASC-Citrine mouse model, two recent reports have identified ASC specks in the
291 cerebellum during development (12) and in retinal astrocytes during ocular hypertension injury
292 (31). Notably, one of the studies also showed the ASC specks in naïve animals (12), mirroring
293 our finding of ASC specks in naïve SC (**Fig. *1D, F***). Further, the ASC specks in the study are
294 AIM2-dependent, and the AIM2 inflammasome contributes to normal brain development (12).
295 Therefore, the function of the AIM2 inflammasome in the CNS may be intrinsically different from
296 that in peripheral myeloid cells, which are equipped to induce inflammation. For example, our
297 study indicated that astrocytes express little *Il1b* mRNA and exhibit no marked cell death upon
298 inflammasome activation in EAE, suggesting that inflammasome activation in astrocytes *in vivo*
299 may have biological implications other than enhancing inflammation.
300   In this study, we observed ASC strings, which were unique to the CNS *in vivo.* However,
301 some *ex vivo* studies have shown a similar ASC string-like structure. "ASC filaments" have been
302 documented *ex vivo* with mutant ASC (32) or with ASC CARD domain blockade or deletion (33-
303 35). An ASC isoform (ASC-c) also generates ASC filaments in human cells and appears to be
304 expressed in mice, at least in the J774A.1 cell line (36). It is not known how astrocytes generate
305 ASC strings, but several possibilities exist, such as potential astrocyte-specific expression of the
306 ASC-c isoform or interaction of inflammasome components with astrocyte-specific molecules. For
307 example, GFAP and vimentin bind together as part of the astrocyte intermediate filament network
308 (37); and vimentin is known to interact with inflammasome components, such as caspase-1 (38).
309 Thus, a possible physical association of GFAP to inflammasome components might explain the
310 appearance of ASC strings in the highly ramified astrocyte.
311   We identified activated caspase-3 in astrocytes with ASC specks in the absence of cell
312 death. Caspases, including caspase-3, possess critical functions outside of induction of cell death
313 (39). Specifically, non-apoptotic caspase-3 activation is involved in the differentiation of numerous
314 cell types, such as monocytes, neurons, and hematopoietic stem cells (39). Also, neurons, which
315 derive from similar progenitors to astrocytes, rely on caspase-3 for dendrite and axon remodeling
316 (40, 41) and synaptic plasticity (42). Caspase-3 activation in astrocytes is also associated with
317 astrogliosis and not cell death (43-46). Specifically, caspase-3 activation in astrocytes is
318 associated with cytoskeletal remodeling in a kainic-acid induced neurodegeneration model (44),
319 reactive astrocytes following excitotoxic N-Methyl-D-aspartate (NMDA)-induced
320 neurodegeneration (46), and GFAP cleavage in an Alzheimer's disease model (43). Indeed, our
321 data suggested the involvement of AIM2 inflammasome in caspase-3 activation and GFAP
322 cleavage. The non-apoptotic activation of caspase-3 in astrocytes is inducible *in vitro*, and

323 promotes expression of glutamate synthase and basic fibroblast growth factor-mediated by
324 astrogliosis (45). Our study now connects inflammasome activation in astrocytes to caspase-3
325 activation and so warrants further study into the role of caspase-3 in astrogliosis.
326   The AIM2 inflammasome is activated by double-stranded DNA (dsDNA) derived not only
327 from microbes but also from endogenous sources as a sentinel of genotoxic stress and DNA
328 damage. The AIM2 inflammasome protects from gastrointestinal toxicity and hematopoietic failure
329 in total-body irradiation (47), which triggers DNA double-strand breaks (47) and nuclear
330 membrane disruption (48). Indeed, the detection of dsDNA by AIM2 is required for normal
331 neurodevelopment during periods of proliferative stress in neurons of the CNS (12). These studies
332 demonstrated AIM2-mediated protection from damage and even limiting inflammation, which
333 positions the AIM2 inflammasome separately from the classical understanding of other
334 inflammasomes, such as the NLRP3 inflammasome. Opposing outcomes of EAE severity in the
335 absence of AIM2 versus ASC, as well as our results demonstrating a detrimental role of ASC in
336 non-hematopoietic cells (**Fig. 2*A-C***), are intriguing; however perhaps not surprising, as ASC is
337 the common adaptor to other inflammasomes, including the NLRP3 inflammasome, which is
338 pathogenic during EAE. Thus, the pathogenic impact of the NLRP3 inflammasome (and perhaps
339 the Pyrin inflammasome (49)) on EAE potentially supersedes the functions of the AIM2
340 inflammasome in an ASC-deficient animal.
341   In conclusion, our study demonstrates astrocyte AIM2 inflammasome activation without
342 eliciting IL-1β-mediated inflammation in the late phase of EAE. This study expands our
343 understanding of astrocytes in EAE and warrants further investigation of non-inflammatory
344 functions of the AIM2 inflammasome in astrocytes during neuroinflammation.
345
346
347 **MATERIALS AND METHODS**
348
349 **Animals.** We used mice of the C57BL/6 genetic background of both sexes aged 8-12 weeks old,
350 unless otherwise noted. Because we did not identify sex differences in our experiments, both
351 male and female were equally represented in our experiments. The ASC-Citrine mice were
352 generated and gifted by Dr. Douglas Golenbock (University of Massachusetts Medical School).
353 The *Pycard*^{-/-} and *Nlrp3*^{-/-} mice were initially obtained from Genentech. The following mice are
354 from The Jackson Laboratory; *Cx3cr1*[CreERT2] (#020940) *Gfap*[Cre] (#012886), *Asc-Citrine*[LSL]
355 (#030743), *Syn1*[Cre] (#003966), and *Aim2*^{-/-} (# 013144). *Gfap*[Cre] and *Syn1*[Cre] mice were used as
356 heterozygotes. Mice for all experiments were housed in a specific pathogen-free environment. All
357 animal experiments included in this study were approved by the Institutional Animal Care and Use
358 Committee of Duke University.
359
360 **EAE induction and scoring.** Mice were immunized with CFA/MOG emulsion in the lower back
361 on day 0. The emulsion was prepared by mixing MOG_{35-55} peptide (United Biosystems, Cat#
362 U104628) and complete Freund's adjuvant (Sigma-Aldrich, Cat# F5881) with additional *Mtb* (BD
363 Difco, Cat# 231141; 200 μg/mouse). The mice also received an intraperitoneal injection of
364 Pertussis toxin (PTx) (200ng/mouse) (List Biological Technologies, Cat# 180) on Day 0 and 2.
365 Unless otherwise noted, we induced EAE with this method, as "Type-A EAE" (100 μg MOG_{35-}
366 $_{55}$/mouse and 200 μg *Mtb*/mouse)(9). In some experiments, "Type-B EAE" (9) was induced with
367 CFA/MOG injection on day 0 and 7 (100 μg MOG_{35-55}/mouse, 400 μg *Mtb*/mouse) and PTx (200
368 ng/mouse) on day 0, 2, and 7. EAE was scored as previously described (2, 3, 9).
369
370 **Preparation of frozen tissue sections and staining with antibodies.** Animals were lethally
371 anesthetized with 100 mg/kg of Nembutal administered intraperitoneally and transcardially
372 perfused with PBS and subsequently 4% paraformaldehyde (PFA)(Sigma-Aldrich, Cat# 158127).
373 SC and iLNs were harvested and fixed for 24 hours at 4°C in 4% PFA. All tissues were

374 cryoprotected in 30% sucrose in water for an additional 24 hours before embedding and freezing
375 in Tissue-Tek O.C.T. compound (Sakura, Cat# 4583) on dry ice. Tissues were sectioned using a
376 Cryostar NX50 (Thermo Fisher Scientific) at a thickness of 25 µm and rendered as floating
377 sections. Sections were permeabilized with 0.25 % Triton X100 (Amresco, Cat# 0694-1L) and
378 blocked using 2% bovine serum albumin (GeminiBio / Cat# 700-101P). After antibody staining,
379 sections were mounted onto slides with ProLong™ Gold Antifade Mountant (Invitrogen, Cat#
380 P36931) or ProLong™ Gold Antifade Mountant with DAPI (Invitrogen, Cat# P36930). TUNEL
381 staining was also performed with 25 µm thick floating tissue sections with the CF 640R TUNEL
382 Assay Apoptosis Detection Kit (Biotium, Cat# 30074). Antibodies used for staining are indicated
383 in **Supplementary Table 1.**

385 **Preparation of tissue slice culture and anti-ASC immunostaining.** Spleens were dissected
386 out of mice, and live spleen slices were prepared with a vibratome (Precisionary Compresstome)
387 using 4% low melt agarose as described by manufacturer's protocol. Slices in complete RPMI
388 were kept as floating sections and treated with 100 ng/mL Ultrapure LPS (Invivogen, Cat# tlrl-
389 3pelps) for 2 hours followed by 5 µM nigericin (Sigma-Aldrich, Cat# N7143) for additional 1 hour.
390 After fixation and permeabilization with ice cold methanol for 15 minutes, slices were blocked with
391 2% BSA in PBS for 1 hour at RT. Immunofluorescence staining was performed with antibodies
392 listed in **Table S1**.

394 **Immunofluorescence microscopy and image analyses.** All slides were imaged on the Zeiss
395 710 Inverted Laser Scanning Confocal Microscope (Duke University Light Microscopy Core
396 Facility) at full 25 µm depth as z-stacks. For quantifications, 2 sections per animal were imaged,
397 and a 2x2 grid tile scan was performed using the 20x objective centered on the ventral horn of
398 the SC, totaling 8 fields per mouse. Following quantification, these replicates were averaged to
399 generate a single *n* for statistical analyses. Semi-automated quantification was conducted using
400 the Imaris for Neuroscientists Cell Imaging Software ver. 9.3.0. (Bitplane) unless otherwise
401 indicated. Briefly, the Surfaces tool was used to identify either ASC specks/strings or cells, and
402 intensity thresholds of counterstain signals within the surfaces were used to quantify the desired
403 characteristics. ASC specks and ASC strings counts in **Fig. 1** were manually enumerated using
404 the LSM Browser software (Zeiss).

406 **Bone Marrow Chimeras.** Recipient mice (CD45.2; 6-8 weeks old) were lethally irradiated with
407 900 rad (XRAD 320 X-Ray irradiator) and adoptively transferred with 10^6 CD45.1 donor bone
408 marrow (BM) cells. Mice were supported with water containing sulfamethoxazole and
409 trimethoprim for 1 week following irradiation. At 6 weeks post-adoptive transfer, the donor cell
410 reconstitution was confirmed by differential expression of congenic markers in peripheral blood
411 using the BD FACSCanto II (BD Biosciences).

413 **Tamoxifen pulse for selective microglial labeling.** This procedure was adapted from previous
414 work (50). Briefly, mice with *Cx3cr1^{CreERT2}* (6-8 weeks old) received an intraperitoneal injection of
415 75 mg/kg tamoxifen dissolved in corn oil. The second injection with the same formula was
416 administered two days later. Mice were kept for six weeks after the last tamoxifen administration
417 for six weeks before EAE induction.

419 **Astrocyte isolation and RT-qPCR.** Astrocytes were isolated as previously described (51) with a
420 few modifications. Briefly, mouse SC were minced into ~1mm^2 pieces and digested using the
421 Papain Dissociation System (Worthington Biochemical Corporation, Cat# LK003153). Isolated
422 cells were negatively selected tandemly first with Myelin Removal Beads II (Miltenyi Biotec, Cat#
423 130-096-731) and second with anti-CD11b MicroBeads (Miltenyi Biotec, Cat# 130-049-601) to
424 collect the flowthrough fraction. To enrich astrocytes, the flowthrough cells were first treated with

FcBlock (Miltenyi Biotec, Cat# 130-092-575), then positively selected using anti-ACSA-2 MicroBeads (Miltenyi Biotec, Cat# 130-097-678). Total RNA was prepared using TRI Reagent (Millipore-Sigma, Cat# 93289) and reverse-transcribed using qScript cDNA Mix (Quantabio, Cat# 950048) to obtain cDNA. RT-qPCR assays were performed with SYBR FAST qPCR Master Mix (Kapa Biosystems, Cat# KK4602), using primers indicated in **Supplementary Table 2**. Expression levels of target genes relative to an internal control, *Actb,* were calculated using the – *ΔΔCt* method (52).

Cell culture and Western blotting analysis. BMDMs were generated by culturing total BM cells for 7 days in complete RPMI supplemented with 10 ng/mL recombinant mouse M-CSF (BioLegend, Cat# 576406M-CSF). C8-S cells (ATCC, Cat# CRL-2535) were cultured in complete DMEM. One day before stimulation, BMDMs and C8-S cells were seeded into poly-L-lysine-coated 12-well plates (1.5×10^6 cells/well). Then, cells were pre-treated with 100 ng/mL Ultrapure LPS (Invivogen, Cat# tlrl-3pelps) in serum-free Opti-MEM medium (Thermo Fisher Scientific, Cat# 11058021) for 2 hours and stimulated with 5 µM nigericin (Sigma-Aldrich, Cat# N7143) or poly(dA:dT) (InvivoGen, Cat# tlrl-patn) for 4 hours to activate the NLRP3 and AIM2 inflammasomes, respectively. Poly(dA:dT) was used as a complex with Lipofectamine 2000 (InvitroGen, Cat# 11668019) at a concentration of 0.5 µg/mL. Culture supernatants and cell lysates (in RIPA buffer) were harvested and, total protein concentrations were quantified using the BCA Protein Assay Kit (ThermoFisher Scientific, Cat# 23227). The same amount of total protein was used across all samples for SDS-PAGE gel separation. Western blotting (WB) was performed with indicated antibodies (**Supplementary Table 1**), and the result was imaged using the GeneGnome Chemiluminescence System (Syngene) and the Genesys (Syngene) software. Band intensity was quantified using the Genetools (Syngene) Software. Lysate β-actin band intensity was used to normalize both the lysate and supernatant band intensity.

Statistical Analyses
Area under the curve (AUC) values were used to statistically analyze EAE scoring data. The Mann-Whitney U-test was used to compare between two groups, unless otherwise indicated. Pre-peak and post-peak AUC were defined by identifying the dpi at which disease score ceased to increase or began to decrease for both groups in a single experiment. All other analyses, where indicated in the figure legend, were performed using either the Mann-Whitney U-test, a One-Factor ANOVA, or a Two-Factor ANOVA. Post-hoc testing was performed only if ANOVA reached significance on interaction term ($p < 0.1$). The Dunnett's Multiple Comparisons and the Sidak's multiple comparisons were conducted post-hoc where indicated in the figure legend. All statistical analyses were performed using the Graphpad Prism 8 software.

Author Contributions: W.E.B., M.E.D., and M.L.S. designed research; W.E.B., M.E.D., M.I., T.N., K.N., N.A.L., and N.A. performed experiments, W.E.B. M.E.D., and M.L.S. analyzed data; W.E.B. and M.L.S wrote the manuscript; and M.E.D., M.I., K.N., N.A.L., N.A. and E.A.M. edited the manuscript.

Data Availability: All study data are included in the article and/or *SI Appendix*.

480

481 **Footnotes:**
482 ↵[1]To whom correspondence may be addressed. Email: mari.shinohara@duke.edu
483 **AIM2**

484

485

486

487 **REFERENCES**

488

489 1. P. Broz, V. M. Dixit, Inflammasomes: mechanism of assembly, regulation and signalling. *Nat Rev*
490 *Immunol* **16**, 407-420 (2016).

491 2. M. Inoue, K. L. Williams, M. D. Gunn, M. L. Shinohara, NLRP3 inflammasome induces
492 chemotactic immune cell migration to the CNS in experimental autoimmune encephalomyelitis.
493 *Proc Natl Acad Sci U S A* **109**, 10480-10485 (2012).

494 3. M. Inoue *et al.*, Interferon-beta therapy against EAE is effective only when development of the
495 disease depends on the NLRP3 inflammasome. *Sci Signal* **5**, ra38 (2012).

496 4. D. Gris *et al.*, NLRP3 plays a critical role in the development of experimental autoimmune
497 encephalomyelitis by mediating Th1 and Th17 responses. *J Immunol* **185**, 974-981 (2010).

498 5. W. Barclay, M. L. Shinohara, Inflammasome activation in multiple sclerosis and experimental
499 autoimmune encephalomyelitis (EAE). *Brain Pathol* **27**, 213-219 (2017).

500 6. L. Vidmar *et al.*, Multiple Sclerosis patients carry an increased burden of exceedingly rare genetic
501 variants in the inflammasome regulatory genes. *Sci Rep* **9**, 9171 (2019).

502 7. S. Malhotra *et al.*, NLRP3 polymorphisms and response to interferon-beta in multiple sclerosis
503 patients. *Mult Scler* **24**, 1507-1510 (2018).

504 8. S. Malhotra *et al.*, NLRP3 inflammasome as prognostic factor and therapeutic target in primary
505 progressive multiple sclerosis patients. *Brain* 10.1093/brain/awaa084 (2020).

506 9. M. Inoue *et al.*, An interferon-beta-resistant and NLRP3 inflammasome-independent subtype of
507 EAE with neuronal damage. *Nat Neurosci* **19**, 1599-1609 (2016).

508 10. M. T. Heneka *et al.*, NLRP3 is activated in Alzheimer's disease and contributes to pathology in
509 APP/PS1 mice. *Nature* **493**, 674-678 (2013).

510 11. B. Hou *et al.*, Inhibition of the NLRP3-inflammasome prevents cognitive deficits in experimental
511 autoimmune encephalomyelitis mice via the alteration of astrocyte phenotype. *Cell Death Dis* **11**,
512 377 (2020).

513 12. C. R. Lammert *et al.*, AIM2 inflammasome surveillance of DNA damage shapes
514 neurodevelopment. *Nature* **580**, 647-652 (2020).

515 13. C. Ma *et al.*, AIM2 controls microglial inflammation to prevent experimental autoimmune
516 encephalomyelitis. *J Exp Med* **218** (2021).

517 14. B. A. McKenzie *et al.*, Activation of the executioner caspases-3 and -7 promotes microglial
518 pyroptosis in models of multiple sclerosis. *J Neuroinflammation* **17**, 253 (2020).

519 15. B. A. McKenzie *et al.*, Caspase-1 inhibition prevents glial inflammasome activation and pyroptosis
520 in models of multiple sclerosis. *Proc Natl Acad Sci U S A* **115**, E6065-E6074 (2018).

16. T. Zeis *et al.*, Metabolic gene expression changes in astrocytes in Multiple Sclerosis cerebral cortex are indicative of immune-mediated signaling. *Brain Behav Immun* **48**, 313-325 (2015).

17. L. Freeman *et al.*, NLR members NLRC4 and NLRP3 mediate sterile inflammasome activation in microglia and astrocytes. *J Exp Med* **214**, 1351-1370 (2017).

18. T. C. Tzeng *et al.*, A Fluorescent Reporter Mouse for Inflammasome Assembly Demonstrates an Important Role for Cell-Bound and Free ASC Specks during In Vivo Infection. *Cell Rep* **16**, 571-582 (2016).

19. G. C. Furtado *et al.*, Swift entry of myelin-specific T lymphocytes into the central nervous system in spontaneous autoimmune encephalomyelitis. *J Immunol* **181**, 4648-4655 (2008).

20. M. van Zwam *et al.*, Surgical excision of CNS-draining lymph nodes reduces relapse severity in chronic-relapsing experimental autoimmune encephalomyelitis. *J Pathol* **217**, 543-551 (2009).

21. M. J. C. Jordao *et al.*, Single-cell profiling identifies myeloid cell subsets with distinct fates during neuroinflammation. *Science* **363** (2019).

22. R. Brambilla, The contribution of astrocytes to the neuroinflammatory response in multiple sclerosis and experimental autoimmune encephalomyelitis. *Acta Neuropathol* **137**, 757-783 (2019).

23. G. Ponath, C. Park, D. Pitt, The Role of Astrocytes in Multiple Sclerosis. *Front Immunol* **9**, 217 (2018).

24. M. Pekny, M. Pekna, Astrocyte reactivity and reactive astrogliosis: costs and benefits. *Physiol Rev* **94**, 1077-1098 (2014).

25. M. V. Sofroniew, H. V. Vinters, Astrocytes: biology and pathology. *Acta Neuropathol* **119**, 7-35 (2010).

26. S. A. Liddelow *et al.*, Neurotoxic reactive astrocytes are induced by activated microglia. *Nature* **541**, 481-487 (2017).

27. N. Itoh *et al.*, Cell-specific and region-specific transcriptomics in the multiple sclerosis model: Focus on astrocytes. *Proc Natl Acad Sci U S A* **115**, E302-E309 (2018).

28. F. Haroon *et al.*, Gp130-dependent astrocytic survival is critical for the control of autoimmune central nervous system inflammation. *J Immunol* **186**, 6521-6531 (2011).

29. W. C. Chou *et al.*, AIM2 in regulatory T cells restrains autoimmune diseases. *Nature* 10.1038/s41586-021-03231-w (2021).

30. C. J. Zhang *et al.*, TLR-stimulated IRAKM activates caspase-8 inflammasome in microglia and promotes neuroinflammation. *J Clin Invest* **128**, 5399-5412 (2018).

31. A. Pronin *et al.*, Inflammasome Activation Induces Pyroptosis in the Retina Exposed to Ocular Hypertension Injury. *Front Mol Neurosci* **12**, 36 (2019).

32. A. C. Sahillioglu, F. Sumbul, N. Ozoren, T. Haliloglu, Structural and dynamics aspects of ASC speck assembly. *Structure* **22**, 1722-1734 (2014).

33. M. Moriya *et al.*, Role of charged and hydrophobic residues in the oligomerization of the PYRIN domain of ASC. *Biochemistry* **44**, 575-583 (2005).

34. A. Lu *et al.*, Unified polymerization mechanism for the assembly of ASC-dependent inflammasomes. *Cell* **156**, 1193-1206 (2014).

35. F. I. Schmidt *et al.*, A single domain antibody fragment that recognizes the adaptor ASC defines the role of ASC domains in inflammasome assembly. *J Exp Med* **213**, 771-790 (2016).

36. N. B. Bryan *et al.*, Differential splicing of the apoptosis-associated speck like protein containing a caspase recruitment domain (ASC) regulates inflammasomes. *Journal of inflammation (London, England)* **7**, 23 (2010).

566 37.   A. Viedma-Poyatos, Y. de Pablo, M. Pekny, D. Perez-Sala, The cysteine residue of glial fibrillary
567   acidic protein is a critical target for lipoxidation and required for efficient network organization.
568   *Free Radic Biol Med* **120**, 380-394 (2018).

569 38.   G. dos Santos *et al.*, Vimentin regulates activation of the NLRP3 inflammasome. *Nat Commun* **6**,
570   6574 (2015).

571 39.   S. Shalini, L. Dorstyn, S. Dawar, S. Kumar, Old, new and emerging functions of caspases. *Cell
572   Death Differ* **22**, 526-539 (2015).

573 40.   A. Erturk, Y. Wang, M. Sheng, Local pruning of dendrites and spines by caspase-3-dependent
574   and proteasome-limited mechanisms. *J Neurosci* **34**, 1672-1688 (2014).

575 41.   D. J. Simon *et al.*, A caspase cascade regulating developmental axon degeneration. *J Neurosci*
576   **32**, 17540-17553 (2012).

577 42.   Z. Li *et al.*, Caspase-3 activation via mitochondria is required for long-term depression and AMPA
578   receptor internalization. *Cell* **141**, 859-871 (2010).

579 43.   P. E. Mouser, E. Head, K. H. Ha, T. T. Rohn, Caspase-mediated cleavage of glial fibrillary acidic
580   protein within degenerating astrocytes of the Alzheimer's disease brain. *Am J Pathol* **168**, 936-
581   946 (2006).

582 44.   L. Acarin *et al.*, Caspase-3 activation in astrocytes following postnatal excitotoxic damage
583   correlates with cytoskeletal remodeling but not with cell death or proliferation. *Glia* **55**, 954-965
584   (2007).

585 45.   R. Aras, A. M. Barron, C. J. Pike, Caspase activation contributes to astrogliosis. *Brain Res* **1450**,
586   102-115 (2012).

587 46.   S. Villapol, L. Acarin, M. Faiz, B. Castellano, B. Gonzalez, Survivin and heat shock protein 25/27
588   colocalize with cleaved caspase-3 in surviving reactive astrocytes following excitotoxicity to the
589   immature brain. *Neuroscience* **153**, 108-119 (2008).

590 47.   B. Hu *et al.*, The DNA-sensing AIM2 inflammasome controls radiation-induced cell death and
591   tissue injury. *Science* **354**, 765-768 (2016).

592 48.   A. Di Micco *et al.*, AIM2 inflammasome is activated by pharmacological disruption of nuclear
593   envelope integrity. *Proc Natl Acad Sci U S A* **113**, E4671-4680 (2016).

594 49.   A. Dumas *et al.*, The inflammasome pyrin contributes to pertussis toxin-induced IL-1beta
595   synthesis, neutrophil intravascular crawling and autoimmune encephalomyelitis. *PLoS Pathog* **10**,
596   e1004150 (2014).

597 50.   E. G. O'Koren, R. Mathew, D. R. Saban, Fate mapping reveals that microglia and recruited
598   monocyte-derived macrophages are definitively distinguishable by phenotype in the retina. *Sci
599   Rep* **6**, 20636 (2016).

600 51.   L. M. Holt, S. T. Stoyanof, M. L. Olsen, Magnetic Cell Sorting for In Vivo and In Vitro Astrocyte,
601   Neuron, and Microglia Analysis. *Curr Protoc Neurosci* **88**, e71 (2019).

602 52.   K. J. Livak, T. D. Schmittgen, Analysis of relative gene expression data using real-time
603   quantitative PCR and the 2(-Delta Delta C(T)) Method. *Methods* **25**, 402-408 (2001).

604

Figure Legends

Figure 1. Inflammasome activation in the CNS during late EAE (A) EAE disease score of WT (*n*=5) vs. ASC-Citrine mice (*n*=4). Mann-Whitney test of total AUC for disease was used. **(B, C)** Representative images *(B)* and quantification *(C)* of ASC specks in the iLNs of ASC-Citrine mice during EAE. Each datapoint represents a value of an average value from two cross-sections of both iLNs (25 µm thickness) per mouse. *n=5* mice. One-way ANOVA, *p*=0.0006, with Dunnett's multiple comparisons test. Scale bar is 20 µm. **(D)** Representative images of SC from ASC-Citrine mice at indicated time points during EAE. Scale bar is 300 µm. **(E-H)** Representative image *(E, G)* and quantification *(F, H)* of ASC specks *(E, F)* and ASC strings *(G, H)* in SC from ASC-Citrine mice during EAE. Scale bar is 10 µm. Each datapoint represents a value from one mouse (*n*=5). Two coronal cross-sections (25 µm thickness) of L5 SC from one mouse were quantified manually and averaged. One-way ANOVA with Dunnett's multiple comparisons tests *(C, F, H)*. ns *p*>0.05, **p < 0.01, ***p<0.001, ****p<0.0001. Error bars denote mean ± SEM.

Figure 2. No inflammasome activation in hematopoietic cells in the CNS during EAE. **(A)** EAE disease scores of WT (BM donor)→WT (recipient) chimeras vs. WT→*Pycard*$^{-/-}$ chimeras. *n*=7, combined from multiple experiments. **(B, C)** Comparison of EAE disease severity of WT→WT chimeras versus WT→*Pycard*$^{-/-}$ chimeras. Each datapoint represents a value from one mouse (*n*=7), combined from multiple experiments. Area under curve (AUC) quantification of pre-peak disease *(B)*, AUC quantification of post-peak disease *(C)*. **(D, E)** Representative images *(D)* and quantification *(E)* of ASC specks in the iLNs of WT→ASC-Citrine chimeras versus ASC-Citrine→WT chimeras at 3 dpi of EAE. Each datapoint represents a value from one mouse as an average of both iLNs (*n*=4). Mann-Whitney test was used. Scale bar is 20 µm. **(F-H)** Representative images *(F)* and quantification of ASC specks *(G)* and ASC strings *(H)* of SC from WT→ASC-Citrine BM chimeras (*n*=4) versus ASC-Citrine→WT chimeras (*n*=6) at 30-dpi of EAE. Each datapoint represents a value from one mouse. Mann-Whitney test was used (*B, C, E, G, H*). Scale bar is 300 µm. *(B, C, G, H)*. ns *p*>0.05, *p<0.05, **p<0.01, ***p<0.001. Error bars denote mean ± SEM.

Figure 3. Identifying inflammasome activation in CNS cells with an immunofluorescent approach. (A-C) Representative images of ASC specks and strings counter-stained with antibodies against TMEM119 for microglia *(A)*, GFAP for astrocytes *(B)*, and NeuN for neurons *(C)* in SC from naïve versus 30-dpi EAE ASC-Citrine mice. Scale bar is 20 µm. **(D, E)** Quantification of ASC specks *(D)* and ASC strings *(E)* in microglia, astrocytes, and neurons in the ventral horn (VH) of SC from naïve versus 30-dpi EAE ASC-Citrine mice. Two-way repeated measures (RM) ANOVAs were used (main effect of cell type: ****p<0.0001 (D, E)), with Sidak's multiple comparisons test post hoc (#p<0.05, ##p<0.01). **(F)** Relative contribution of microglia, astrocytes and neurons to total number of ASC specks in L5 SC at 30-dpi EAE. "Unassigned" indicates unidentified cell sources of ASC-Citrine signals. Each datapoint represents a value from one mouse (*n*=5). Two-way RM ANOVA was used (main effect of cell type: *p*<0.001) with Sidak's multiple comparisons test post hoc. **p<0.01. Error bars denote mean ± SEM.

Figure 4. Identifying Inflammasome activation in CNS cells by a mouse genetics approach. (A-C) Representative images of SC in *Asc-Citrine*^{LSL} versus *Cx3cr1*^{CreERT2};*Asc-Citrine*^{LSL} mice *(A)*, *Gfap*$^{Cre/+}$;*Asc-Citrine*^{LSL} mice *(B)*, and *Syn1*$^{Cre/+}$;*Asc-Citrine*^{LSL} mice *(C)* at day 30-dpi of EAE. Mice for microglia evaluation were treated with tamoxifen. Scale bar is 20 µm. **(D, E)** Quantification of ASC specks *(D)* and ASC strings *(E)* in SC VH of mice indicated in (A-C). Each datapoint represents a value from one mouse. Combined from multiple experiments. *(D, E)* Mann-Whitney test was used. ****p<0.0001. Error bars denote mean ± SEM.

655

656 **Figure 5. Evaluation of astrocytes with activated inflammasomes. (A, B)** Representative
657 images *(A)* and quantification *(B)* of total GFAP intensity in SC ventral gray matter from naïve 30-
658 dpi EAE mice. Scale bar is 200 µm. GFAP intensity was quantified as mean signal intensity of
659 GFAP in the ventral grey matter (VGM) using ImageJ. Mann-Whitney test was used. **(C-E)**
660 Representative images *(C)* and quantification of GFAP intensity *(D)* and C3d intensity *(E)* per cell
661 in gray matter SC astrocytes with and without ASC specks/strings from naïve ASC-Citrine (*n*=7)
662 mice versus ASC-Citrine mice at 30-dpi of EAE (*n*=6). Scale bar is 200 µm. Each datapoint
663 represents a value from one mouse. Individual astrocytes were identified using the Imaris
664 software and the mean intensity per cell was quantified for GFAP and C3d. Two-way RM ANOVA
665 was used with Sidak's multiple comparisons test post-hoc. **p<0.01. ***p<0.001. Error bars
666 denote mean ± SEM.

667

668 **Figure 6. Outcomes of inflammasome activation in astrocytes. (A, B)** RT-qPCR evaluation
669 of inflammasome-related genes in SC total cells vs. astrocytes isolated from mice with EAE at 30-
670 dpi. Two-way RM ANOVAs were used with Sidak's multiple comparisons test post-hoc. **(C)**
671 Representative images of Western blotting for inflammasome components in BMDMs vs. C8-S
672 cells. Cells in all groups were pre-treated with Ultrapure LPS. Groups in Lane 2 and 3 were further
673 stimulated with nigericin and poly(dA:dT)/liposome to activate the NLRP3 and AIM2
674 inflammasomes, respectively. **(**Cells in Group1 were treated by Ultrapure LPS alone.) **(D, E)**
675 Representative images *(D)* and quantification *(E)* of TUNEL staining of SC sections from naïve
676 (*n*=3) and 30-dpi EAE ASC-Citrine mice (*n*=4). Two-way repeated measures (RM) ANOVAs was
677 used. Scale bar is 75 µm. **(F, G)** Representative images *(F)* and quantification *(G)* of active
678 caspase-3 (CC3) in SC astrocytes with and without ASC specks/strings. Evaluated from naïve
679 (*n*=7) and at 30-dpi EAE (*n*=6) ASC-Citrine mice. Scale bar is 200 µm. Individual astrocytes were
680 identified using the Imaris software and were quantified by CC3 puncta staining. Each datapoint
681 represents a value from one mouse, combined from multiple experiments. Two-way RM ANOVA
682 was used with Sidak's multiple comparison test post-hoc. *(A, B, E, G)* **p<0.01, ***p<0.001,
683 ****p<0.0001. Error bars denote mean ± SEM.

684

685 **Figure 7. AIM2 inflammasome activation in astrocytes during EAE. (A, B)** Comparison of
686 ASC speck formation in indicated mouse groups. Representative images *(A)* and quantification
687 of ASC specks *(B)* of SC sections from ASC-Citrine (*n*=6) versus *Nlrp3*$^{-/-}$ ASC-Citrine (*n*=7) mice
688 at 30-dpi Type B EAE. Mann-Whitney test was used. **(C, D)** EAE disease scores *(C)* and statistical
689 evaluation of AUC *(D)* of WT (*n*=8) versus *Aim2*$^{-/-}$ (*n*=7) mice induced with Type-A EAE with low
690 dose *Mtb* (50 µg/mouse). Mann-Whitney test of AUC was used to analyze post-peak disease *(D)*.
691 **(E)** Quantification of GFAP intensity per cell in gray matter SC astrocytes from WT (*n*=3) versus
692 *Aim2*$^{-/-}$ (n=4) mice at 30-dpi of Type-A EAE with low dose *Mtb* (50 µg/mouse). Unpaired t-test was
693 used. **(F-H)** Type-A EAE with 200 µg *Mtb*/mouse. EAE disease score of ASC-Citrine (*n*=8), *Aim2*$^{+/-}$
694 ;ASC-Citrine (*n*=6), *Aim2*$^{-/-}$; ASC-Citrine (*n*=4) mice *(F)*. Representative images *(G)* and
695 quantification of ASC specks *(H)* of SC sections at 30-dpi EAE. Scale bar is 200µm *(A, G)*. One-
696 way ANOVA was used (*p* < 0.0001) with Dunnet's multiple comparisons test post-hoc *(H)*.
697 Unpaired t-test was used. (*B,D,E*). Each datapoint represents a value from one mouse (*B, D, E,*
698 *H*). *ns*; not significant (*p*>0.05), *p<0.05, **p<0.01. Error bars denote mean ± SEM.

699

700 **Figure S1. Validation of ASC-Citrine system in tissue imaging. (A)** Representative images of
701 ASC speck formation detected with ASC-Citrine and ASC antibody signals. Live spleen tissue
702 culture slices from naïve WT and ASC-Citrine mice were used with NLRP3 inflammasome
703 stimulation. Scale bar is 50 µm. **(B)** Quantification of ASC specks in the iLNs and cLNs of ASC-
704 Citrine mice during EAE. Each datapoint represents a value of an average value from two cross-

705 sections of LNs (25 µm thickness) from one mouse. One-way ANOVA, *p*=0.0021 (iLN), *p*=0.3235
706 (cLN), with Dunnett's multiple comparisons test. **(C, D)** Comparison of ASC speck images and
707 numbers in SC between Type-A and Type-B EAE. Representative images (C) and quantification
708 (D) of ASC specks in the SC of ASC-Citrine mice at 30-dpi for Type A (*n=5*) and Type B (*n=8*)
709 EAE. Each datapoint represents a value from one mouse. Mann-Whitney test was used. Scale
710 bar is 200 µm. (*B,D*) *ns*; not significant (*p*>0.05), **p*<0.05, ***p*<0.01. Error bars denote mean ±
711 SEM.

713 **Figure S2. Validation of Bone Marrow Chimeras.** BM chimera were created by transferring WT
714 BM cells to irradiated WT or *Pycard*$^{-/-}$ receipients (n=*7* for each group). Reconstitution efficiency
715 of BM chimeras determined by flow cytometry, quantified as % of total CD45$^+$ cells in peripheral
716 blood for congenic markers of CD45.1 (donor) or CD45.2 (recipient). Each datapoint represents
717 a value from one mouse. Mann-Whitney test used. **(B, C)** BM chimera were created by
718 transferring ASC-Citrine BM cells irradiated WT recipients (ASC-Citrine → WT, *n*=6) and vice
719 versa (WT → ASC-Citrine mice, *n*=8). Reconstitution efficiency (*B*) and EAE disease score (*C*) of
720 indicated BM chimera Mann-Whitney test of total AUC for disease. **(D)** Representative images of
721 SC from ASC-Citrine → WT mice at indicated time points during EAE. No apparent ASC specks
722 were observed. Scale bar is 500 µm. **(E)** Representative image of ALDH1L1 counterstaining of
723 astrocytes in ASC-Citrine mice at 30-dpi EAE. Scale bar is 10 µm. **(F)** Representative images of
724 ASC specks and strings counter-stained with antibodies against NG2 (for OPCs) and MBP (for
725 mature oligodendrocytes) in SC from naïve versus 30-dpi EAE ASC-Citrine mice. Scale bar is 20
726 µm. **(G)** Quantification of ASC specks in OPCs and mature oligodendrocytes of SC from naïve
727 versus 30-dpi EAE ASC-Citrine mice. Each datapoint represents a value from one mouse. Two-
728 way repeated measures (RM) ANOVA was used (main effect of cell type: ^{ns}p<0.7807). **(H)**
729 Percentages of ASC specks detected in OPC or mature oligodendrocytes out of total ASC specks
730 per section, indicating relative contribution of OPCs and oligodendrocyte ASC specks to total
731 number of ASC specks in L5 spinal cord at 30-dpi EAE. (*A,B,C,G,H*) *ns*; not significant (*p*>0.05).
732 Error bars denote mean ± SEM. **(I)** Percentage of ChAT$^+$ and ChAT$^-$ VH neurons containing
733 ASC specks in SC from naïve vs. 30-dpi EAE ASC-Citrine mice. Each datapoint represents a
734 value from one mouse (n=5). Two-way RM ANOVA was used (main effect of cell type: p<0.001)
735 with Sidak's multiple comparisons test post hoc. ***p*<0.01.

737 **Figure S3. Validation of EAE mice with cell type-specific ASC-Citrine expression. (A)**
738 Tamoxifen mediated expression of ASC-citrine reporter expression in microglia and splenic
739 monocytes in *Cx3cr1*^{CreERT2}*;Asc-Citrine*^{LSL} with or without tamoxifen (TAM) treatment. **(B)** Flow
740 cytometry gating strategy for identifying microglia. **(C)** EAE disease score of *Cx3cr1*^{CreERT2}*;Asc-*
741 *Citrine*^{LSL} (*n=5*) vs. *Cx3cr1*^{CreERT2}*;Asc-Citrine*^{LSL} (*n=5*). Both groups were treated with TAM. **(D, E)**
742 EAE disease score of *Asc-Citrine*^{LSL} (*n=10*) vs. *Gfap*^{Cre}*;Asc-Citrine*^{LSL} (*n=13*) (*D*) and *Asc-*
743 *Citrine*^{LSL} (*n=13*) vs. *Syn1*^{Cre}*;Asc-Citrine*^{LSL} (*n=10*) (E). Mann-Whitney test of total AUC of disease
744 score was used (*C,D,E*). *ns*; not significant (*p*>0.05). Error bars denote mean ± SEM.

746 **Figure S4. Expression of inflammasome components and cell death markers in astrocytes**
747 **during EAE. (A)** Gene-set enrichment analysis of inflammasome-associated genes in bulk SC
748 lysates and astrocytes (with astrocyte-specific Ribotag-HA enriched RNA) in naïve and 30-dpi
749 EAE mice. Data represented as raw transcript counts derived from publicly available data (GEO
750 Accession #: GSE100329). **(B-G)** Representative images (*B-D*) and quantification (*E-F*) of
751 caspase-1 (*B, E*), IL-1β (*C, F*), and GSDMD (*D, G*) expression in spleen and SC astrocytes from

752 naïve versus 30-dpi EAE ASC-Citrine mice. Scale bar is 20 μm. Each datapoint represents a
753 value from one mouse. Individual astrocytes were identified using the Imaris software and the
754 mean intensity per cell was quantified for caspase-1 (*E*), IL-1β (*F*) and GSDMD (*G*). Mann-
755 Whitney test was used. (E-*G*) *ns*; not significant ($p > 0.05$). Error bars denote mean ± SEM.
756
757 **Figure S5. Expression of inflammasome components in C8-S astrocyte cell line (A-C)** WB
758 quantitative evaluation of culture supernatant samples of mature caspase-1 (*A*), IL-1β (*B*), and IL-
759 18 (*C*). **(D-H)** WB quantitative evaluation of cell lysate samples of pro-caspase-1 (*D*), pro-IL-1β
760 (*E*), pro-IL-18 (*F*), GSDMD-FL (*G*), and GSDMD-NT (*H*). In (*A-H*), all groups were stimulated with
761 Ultrapure LPS, and Groups 2 and 3 were further stimulated with nigericin and
762 poly(dA:dT)/liposome to activate the NLRP3 and AIM2 inflammasomes, respectively. (Thus,
763 Group 1 has Ultrapure LPS treatment alone.) Each datapoint is obtained from one independent
764 experiment. Two-way RM ANOVA was used with Sidak's multiple comparison test post-hoc. **(I)**
765 Quantification of active caspase-3 (CC3) in spinal cord astrocytes with and without ASC
766 specks/strings in *Gfap*^Cre*;Asc-Citrine*^LSL^ (*n=6*) mice at 30-dpi EAE. Each datapoint represents a
767 value from one mouse. Individual astrocytes were identified using the Imaris software and were
768 quantified by CC3 puncta staining. Mann-Whitney test was used. (*A-I*) **$p < 0.01$, **$p < 0.005$,
769 ***$p < 0.001$, ****$p < 0.0001$. Error bars denote mean ± SEM.
770
771 **Figure S6. Validation of EAE phenotype of *Nlrp3*^-/-^;ASC-Citrine mice and immune**
772 **phenotype of *Aim2*^-/-^ mice with EAE. (A)** EAE disease score of ASC-Citrine (*n=7*) vs. *Nlrp3*^-/-^
773 ;ASC-Citrine (*n=8*) mice with Type B-EAE. Mann-Whitney test of total AUC for disease score was
774 used. **(B–D)** Leukocyte counts in SC (*B*), iLN (*C*) and spleen (D) at 16-dpi EAE in WT vs. *Aim2*^-/-^
775 mice induced with Type-A EAE. One datapoint represents a value from one mouse. Two-way RM
776 ANOVA was used with Sidak's multiple comparisons test post hoc. **(E)** Representative image of
777 GFAP staining in SC from WT versus *Aim2*^-/-^ mice at 30-dpi of EAE. Scale bar is 200 μm. (*A-D*)
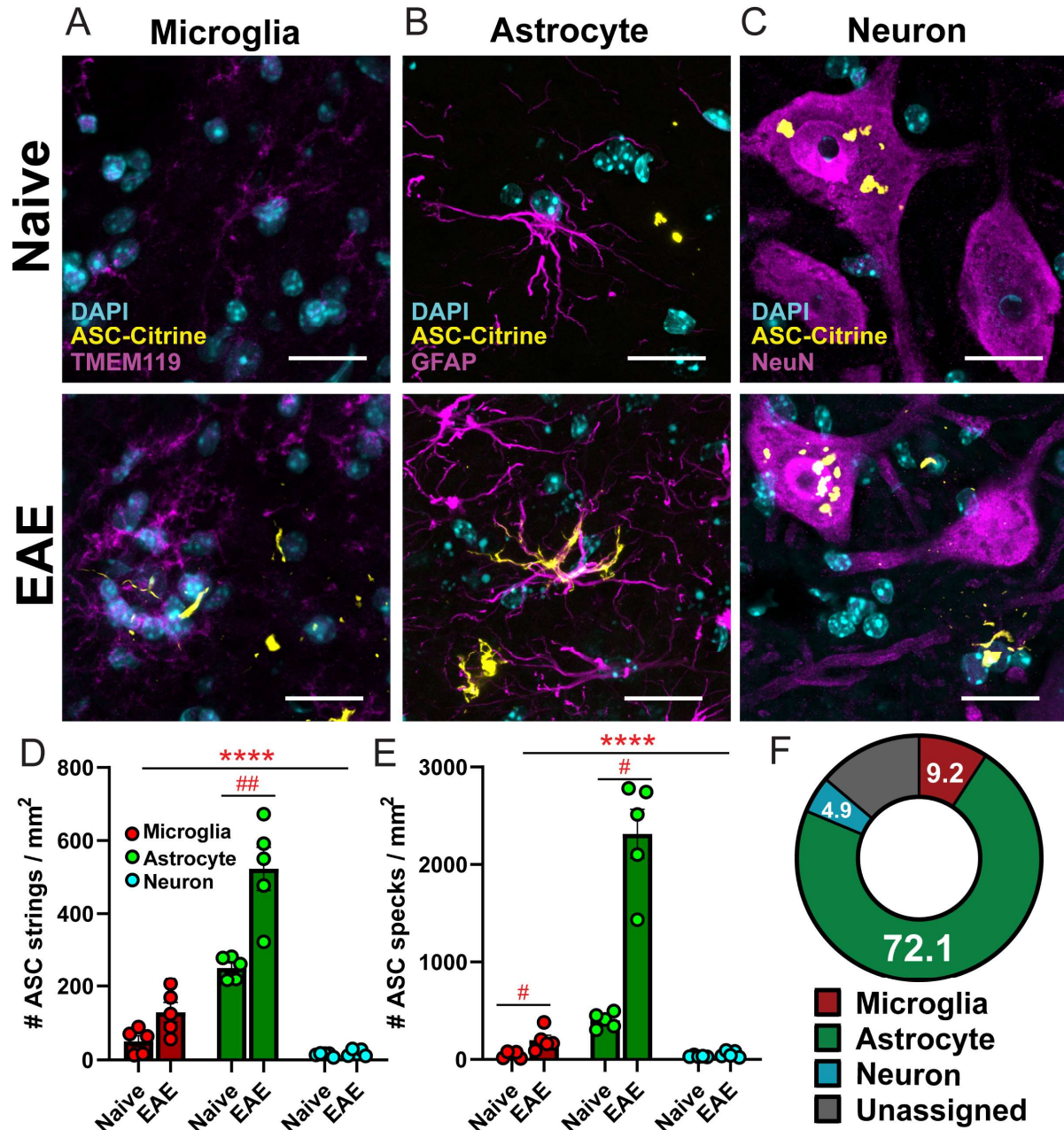778 *ns*; not significant ($p > 0.05$). Error bars denote mean ± SEM.
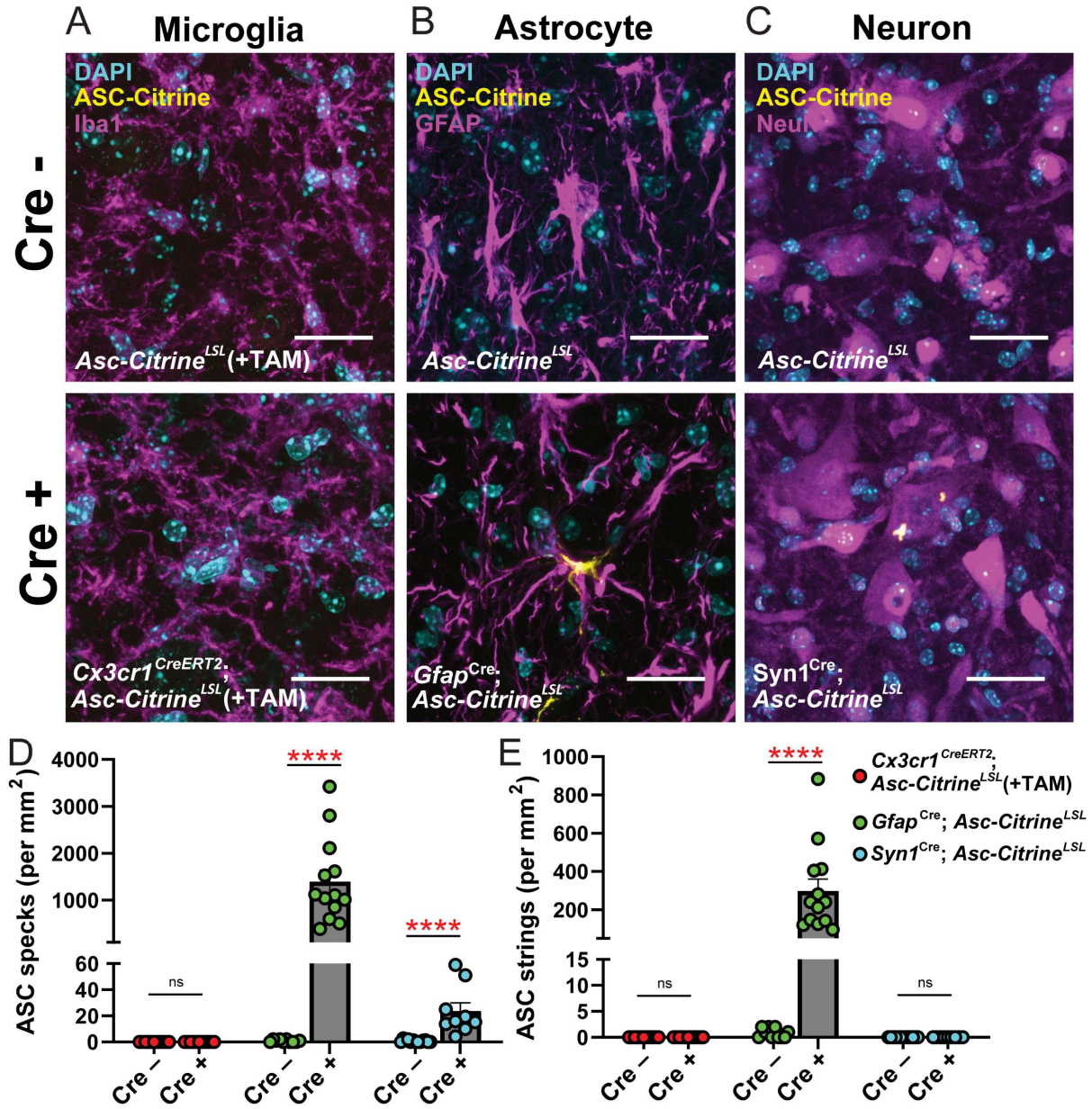779
780
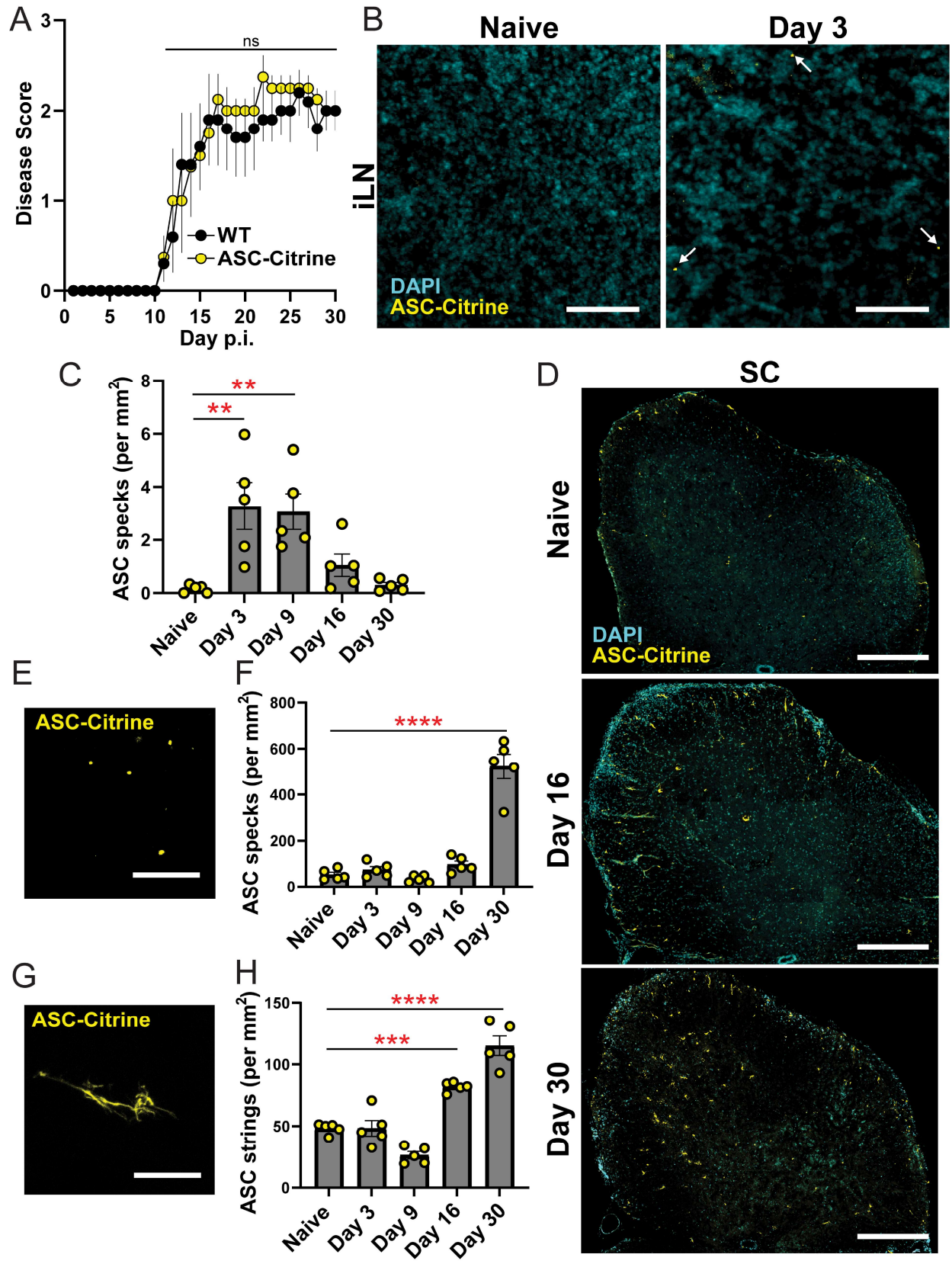
781
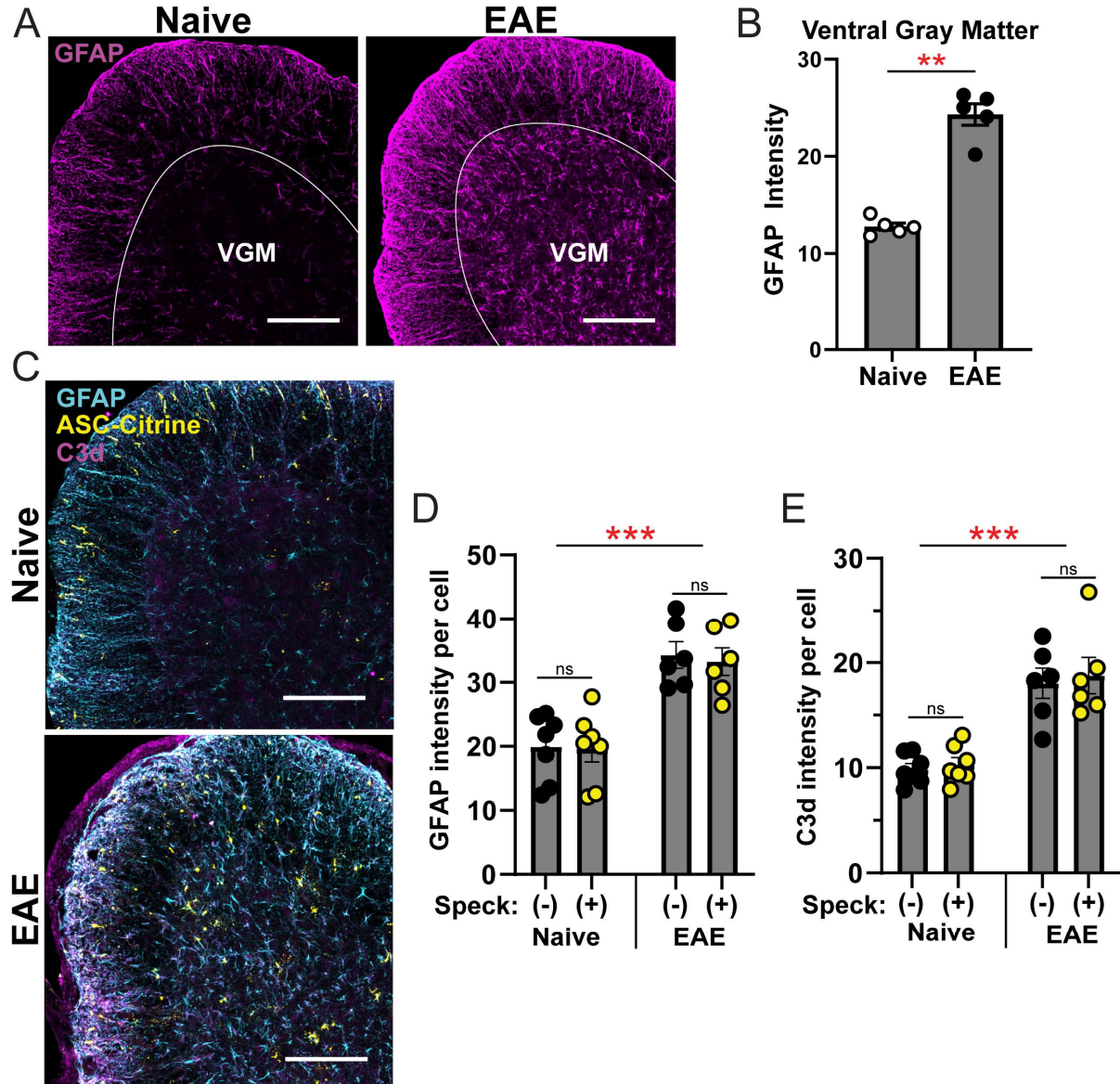782 **Figure 1**
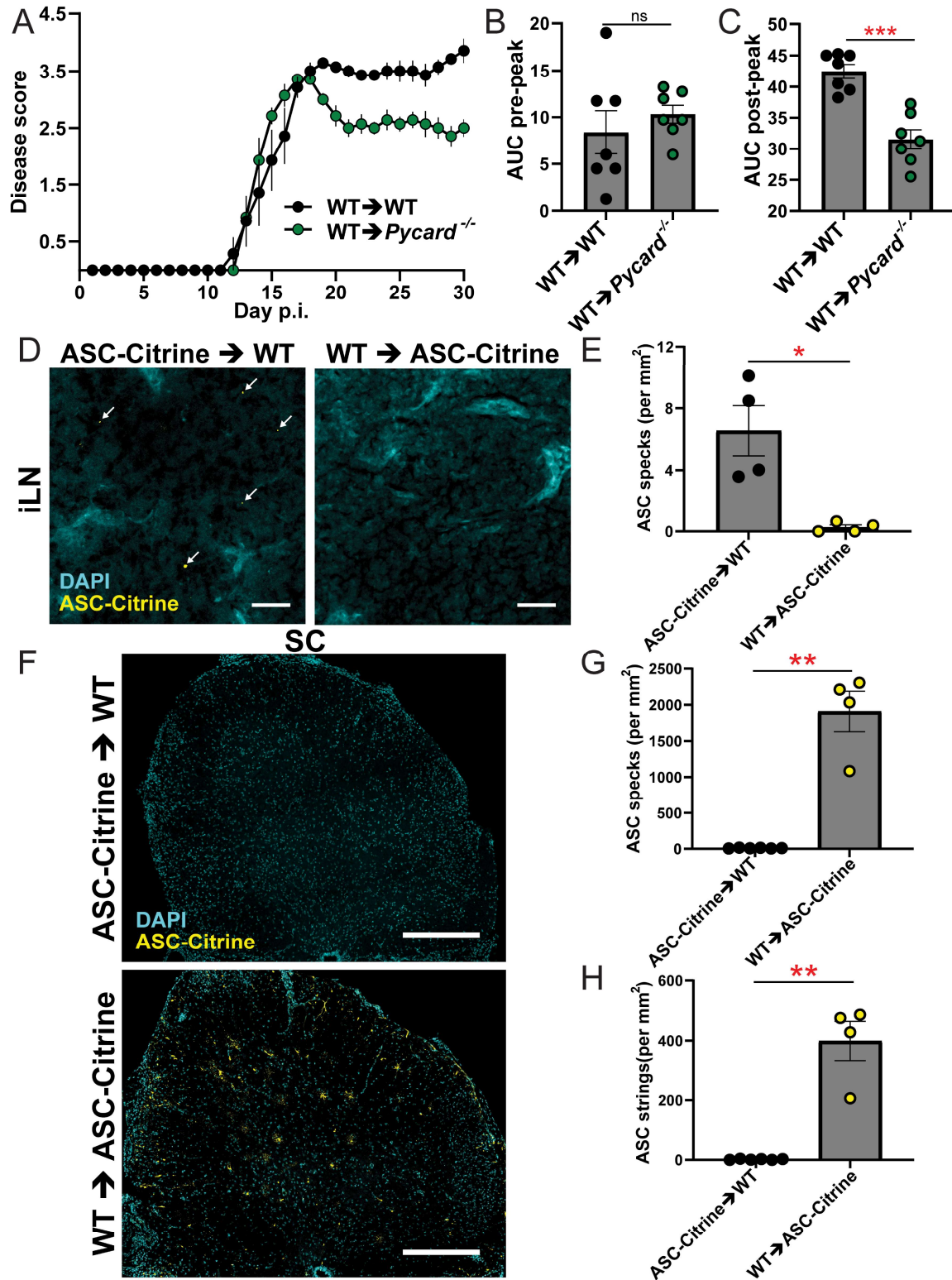
783
784
785   **Figure 2**

786
787
788
789
790
791
792
793
794
795
796 **Figure 3**

797
798
799
800
801
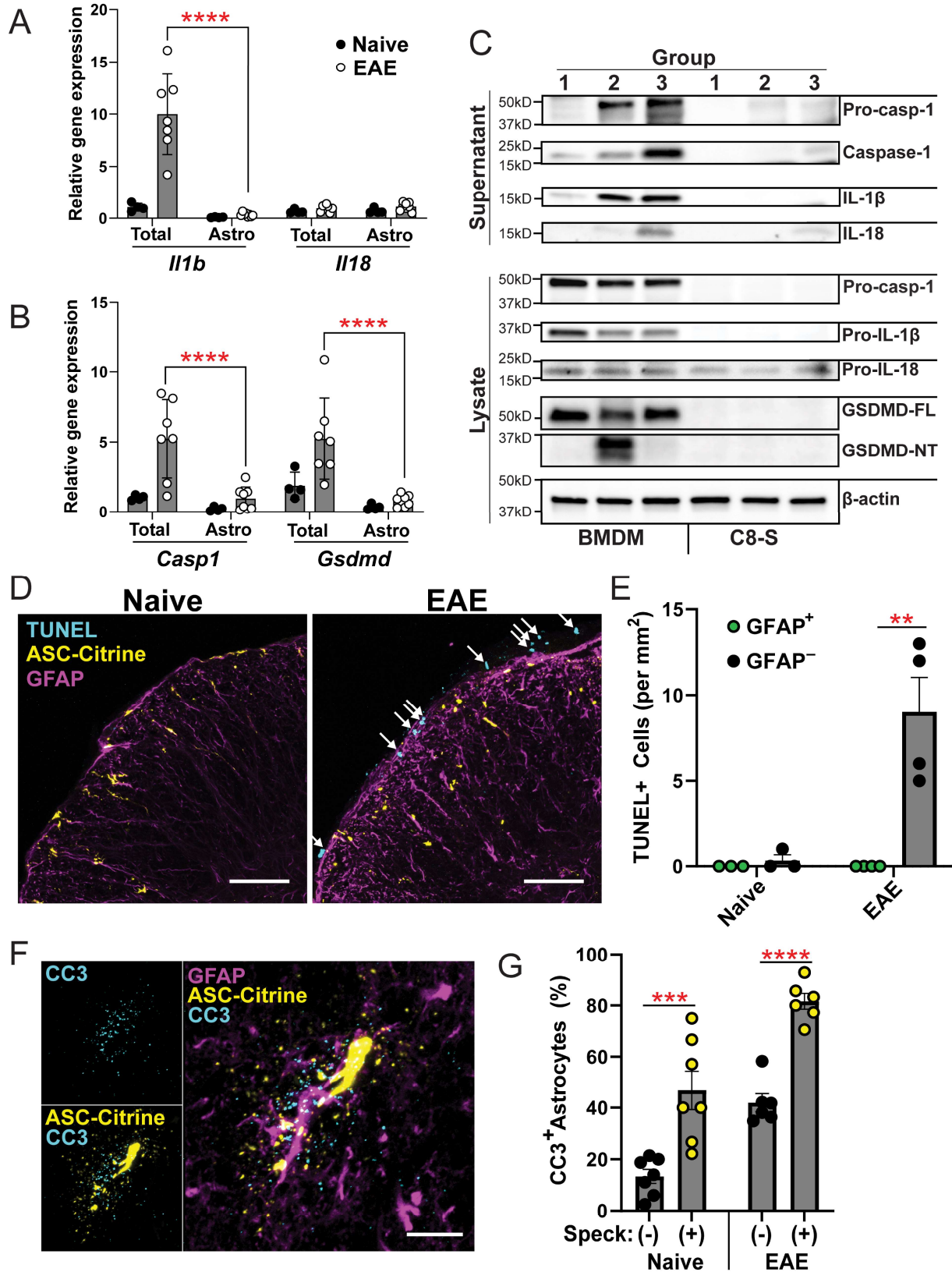802
803
804
805
806
807
808
809
810
811 **Figure 4**

812
813
814
815
816
817
818
819
820
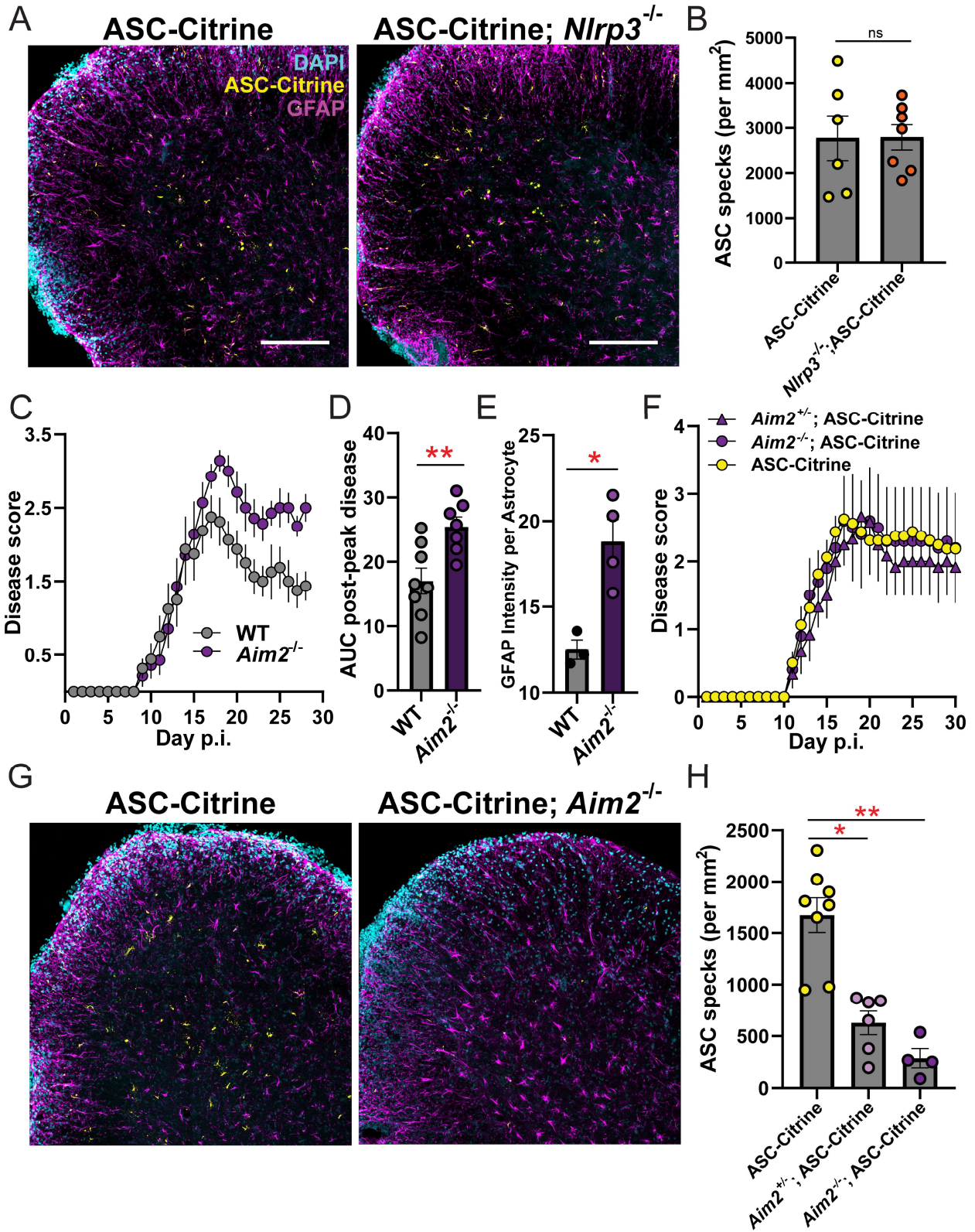821
822
823
824
825
826
827
828 **Figure 5**

829

830
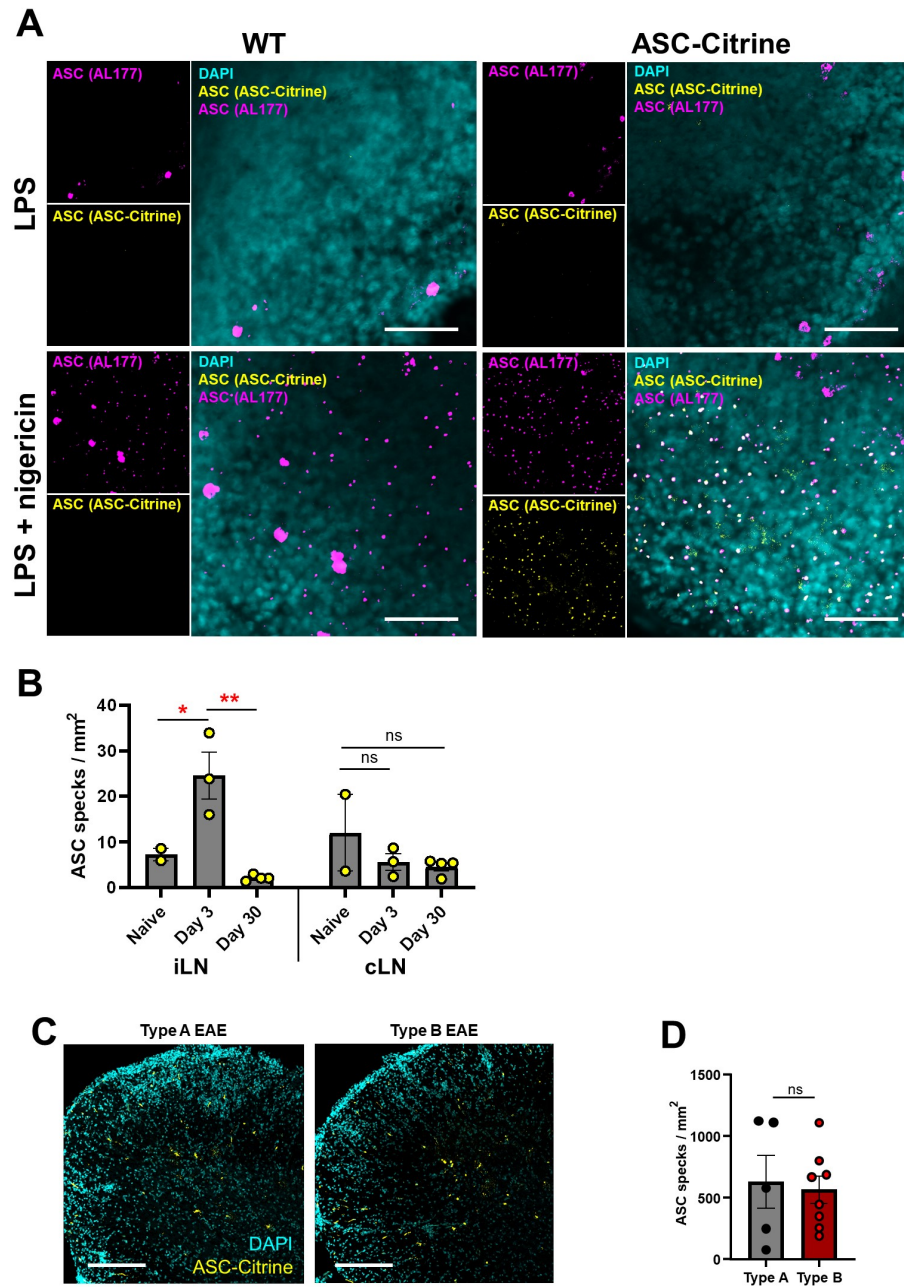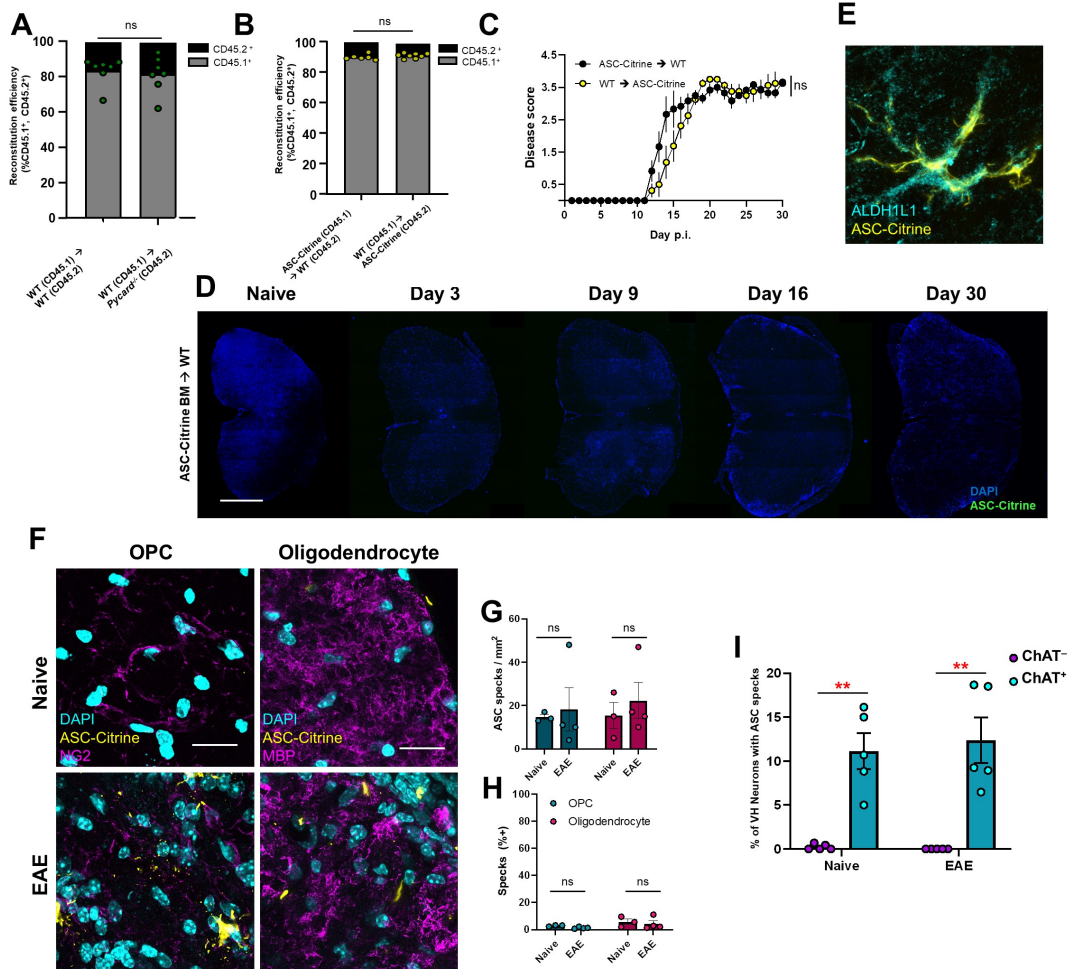831   **Figure 6**

832
833
834
835 **Figure 7**

Figure S1

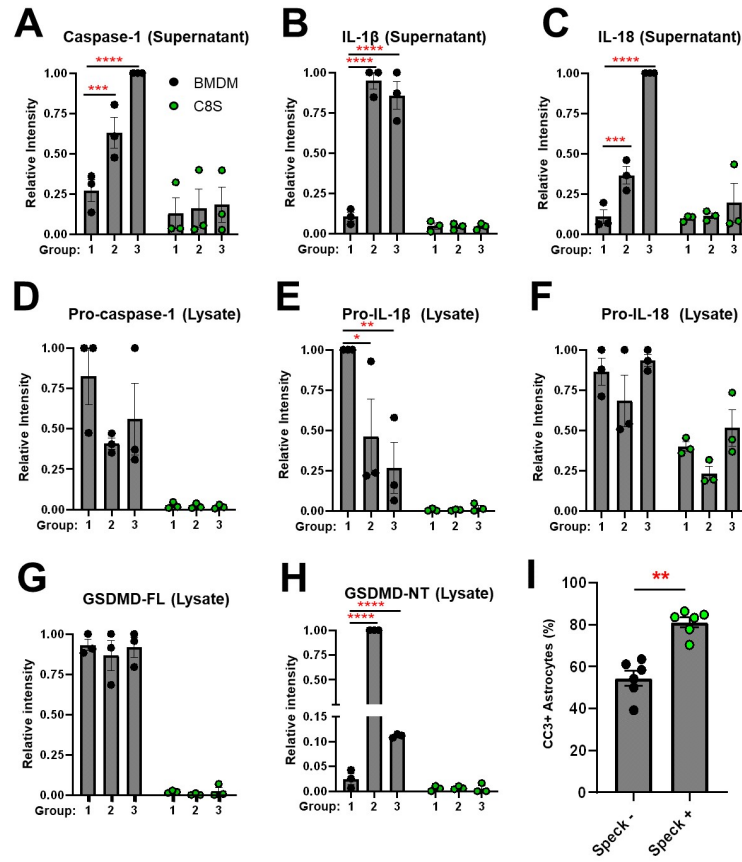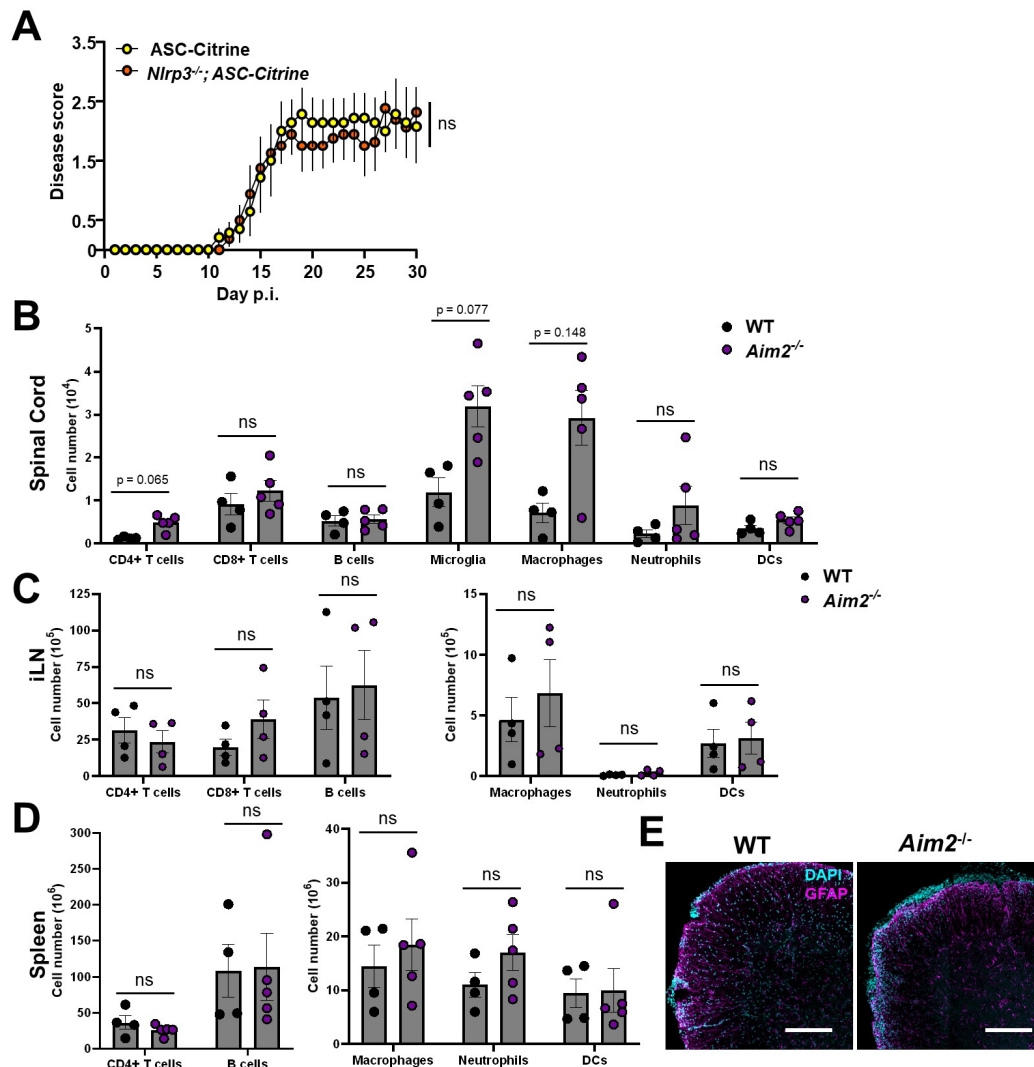**Figure S2**
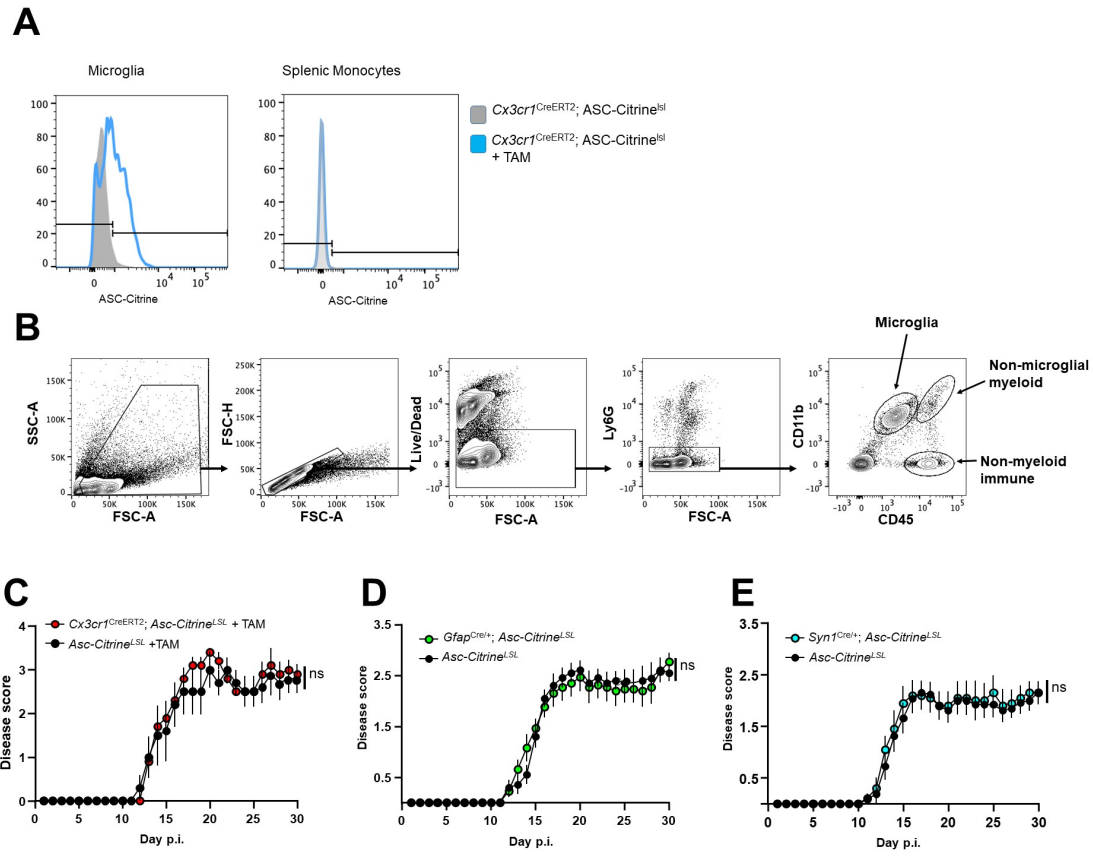
Figure S3
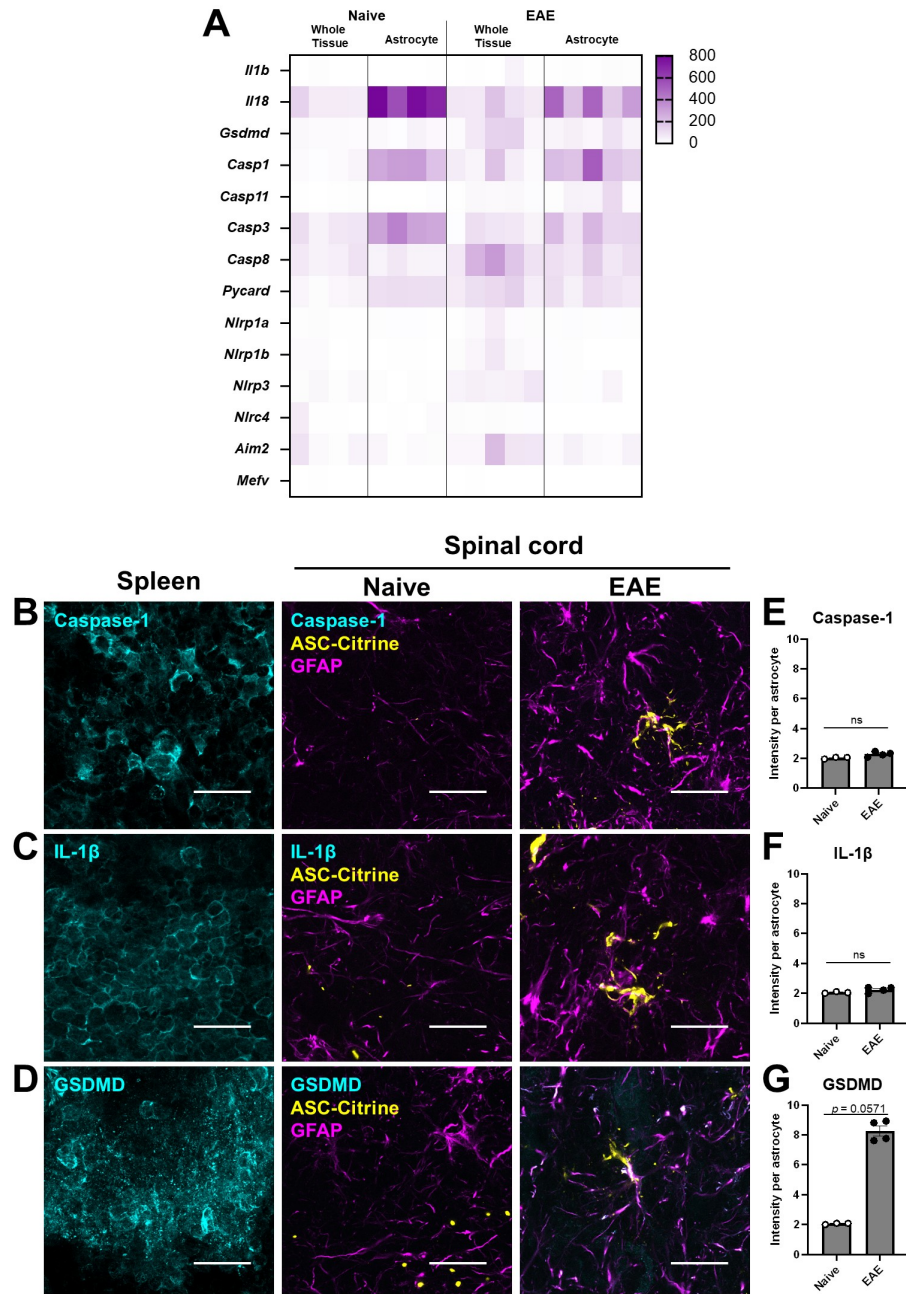
Figure S4

Figure S5

Figure S6

Table S1. Reagent information for antibody-based techniques

Target	Cat #	Species	Clone	Supplier	Dilution	Technique
ASC	AG-25B-0006-C100	Rabbit	AL177, polyclonal	Adipogen	1:500	IF Imaging
Tmem119	ab209064	Rabbit	28-3	Abcam	1:500	IF Imaging
GFAP	13-0300	Rat	2.2B10	Invitrogen	1:500	IF Imaging, Western Blotting
ALDHL1	ab87117	Rabbit	polyclonal	Abcam	1:500	IF Imaging
NeuN	ab104225	Rabbit	polyclonal	Abcam	1:500	IF Imaging
ChAT	AB144P	Goat	polyclonal	EMD Millipore	1:100	IF Imaging
NG2	ab275024	Rabbit	EPR23976-145	Abcam	1:500	IF Imaging
MBP	ab218011	Rabbit	EPR21188	Abcam	1:500	IF Imaging
Iba1	NB100-1028	Goat	polyclonal	Novus Biologicals	1:500	IF Imaging
C3d	AF2655	Goat	polyclonal	R&D Systems	1:500	IF Imaging
Cleaved caspase-3	9664S	Rabbit	5AIE	Cell Signaling Technologies	1:500	IF Imaging
Caspase-1	N/A	Rat	4b4	Genentech	1:500	IF Imaging, Western Blotting
Gasdermin D	PA5-1155330	Rabbit	polyclonal	ThermoFisher Scientific	1:500	IF Imaging
Gasdermin D	ab209845	Rabbit	EPR19828	Abcam	1:500	Western Blotting
IL-1β	AF-401-NA	Goat	polyclonal	R&D Systems	1:1000	IF Imaging, Western Blotting
IL-18	210-401-323	Rabbit	polyclonal	Rockland	1:1000	Western Blotting
CD45.1	110708	Mouse	A20	Biolegend	1:200	Flow Cytometry
CD45.2	109831	Mouse	104	Biolegend	1:200	Flow Cytometry

Table S2. Sequences of primers used for RT-qPCR assays

Gene	Direction	Sequence
Actb	Forward	TGT TAC CAA CTG GGA CGA CA
	Reverse	CTG GGT CAT CTT TTC ACG GT
Casp1	Forward	GAA GGC CCA TAT AGA GAA AGA TTT TAT TG
	Reverse	GAC AGG ATG TCT CCA AGA CAC ATT
Gsdmd	Forward	GCG ATC TCA TTC CGG TGG ACA G
	Reverse	TTC CCA TCG ACG ACA TCA GAG AC
Il1b	Forward	CGC AGC AGC ACA TCA ACA AGA GC
	Reverse	TGT CCT CAT CCT GGA AGG TCC ACG
Il18	Forward	CAG GCC TGA CAT CTT CTG CAA
	Reverse	CTG ACA TGG CAG CCA TTG T